MUCOSAL IMMUNOLOGY

# Microbial energy metabolism fuels an intestinal macrophage niche in solitary isolated lymphoid tissues through purinergic signaling

**Pailin Chiaranunt[1], Kyle Burrows[1], Louis Ngai[1], Siu Ling Tai[1], Eric Y. Cao[1], Helen Liang[1], Homaira Hamidzada[1,2,3], Anthony Wong[1,2,3], Julia Gschwend[4], Pascal Flüchter[4], Meggie Kuypers[1], Tijana Despot[1], Abdul Momen[2,3], Sung Min Lim[1], Thierry Mallevaey[1,5], Christoph Schneider[4], Tyrrell Conway[6], Hiromi Imamura[7], Slava Epelman[1,2,3], Arthur Mortha[1]***



**Maintaining macrophage (MΦ) heterogeneity is critical to ensure intestinal tissue homeostasis and host defense. The gut microbiota and host factors are thought to synergistically guide intestinal MΦ development, although the exact nature, regulation, and location of such collaboration remain unclear. Here, we report that microbial biochemical energy metabolism promotes colony-stimulating factor 2 (CSF2) production by group 3 innate lymphoid cells (ILC3s) within solitary isolated lymphoid tissues (SILTs) in a cell-extrinsic, NLRP3/P2X7R-dependent fashion in the steady state. Tissue-infiltrating monocytes accumulating around SILTs followed a spatially constrained, distinct developmental trajectory into SILT-associated MΦs (SAMs). CSF2 regulated the mitochondrial membrane potential and reactive oxygen species production of SAMs and contributed to the antimicrobial defense against enteric bacterial infections. Collectively, these findings identify SILTs and CSF2-producing ILC3s as a microanatomic niche for intestinal MΦ development and functional programming fueled by the integration of commensal microbial energy metabolism.**



## INTRODUCTION

Intestinal macrophages (MΦs) represent a large proportion of the innate immune system in the gut and are critical mediators of host defense and tissue homeostasis. Although their heterogeneity is widely appreciated, the mechanisms regulating MΦ heterogeneity within microanatomic environments of intestinal lamina propria (LP) remain enigmatic (*1*). Further complicating this matter are the classification strategies for intestinal MΦs. As in other organs, intestinal MΦ subpopulations can be distinguished on the basis of their expression of the markers T cell immunoglobulin and mucin domain containing 4 (Tim-4) and C-C motif chemokine receptor 2 (CCR2) to denote fetal-derived long-lived, self-renewing cells and monocyte-derived ones, respectively (*2*, *3*). Others have demarcated gut MΦs using Tim-4 and CD4 into three subpopulations: Tim-4$^-$CD4$^-$ and Tim-4$^-$CD4$^+$ MΦs with rapid monocytic turnover and long-lived Tim-4$^+$CD4$^+$ MΦs with slow monocytic turnover, each subset capable of associating with either neurons, vasculature, and other immune cells within distinct regions to adopt transcriptional profiles and functions tailored to these microenvironments (*4*, *5*) (*6*–*8*).

In contrast to other organs, intestinal MΦs integrate signaling by microbial metabolites derived from the commensal microflora into their homeostatic function (*7*, *9*). For example, polysaccharides produced by *Helicobacter hepaticus* and commensal bacteria-derived short-chain fatty acids (SCFAs) promote tolerogenic MΦs (*10*–*12*). Bacteria-metabolized dietary tryptophan controls monocyte differentiation in an aryl hydrocarbon receptor–dependent manner (*13*). Colonization with the protozoan commensal *Tritrichomonas musculis* (*T. mu*) was recently shown to induce monocyte infiltration in the gut by increasing luminal extracellular adenosine 5′-triphosphate (ATP) levels (*14*). Collectively, these studies raise the question of whether a ubiquitously produced metabolite conserved across microbial kingdoms may serve as a molecular motif for imprinting MΦ heterogeneity.

Microbiota- and host-derived factors collaborate in orchestrating gut MΦ composition and function. Deficiency in the host-derived myeloid growth factor colony-stimulating factor 1 (CSF1) results in a systemic decrease in MΦs, with a less pronounced effect on the intestinal tract, suggesting compensatory growth factors (*15*–*17*). Interleukin-34 (IL-34), transforming growth factor–β, or CSF2 has been reported to affect MΦ development in many organs, including the intestinal tract (*18*–*20*). In the gut, tissue-resident group 3 innate lymphoid cells (ILC3s) produce large quantities of CSF2 in a microbiota-dependent manner within cryptopatches and isolated lymphoid follicles (ILFs), collectively known as solitary isolated lymphoid tissues (SILTs). CSF2 production in ILC3s was dependent on the IL-1 receptor and MΦ-derived IL-1β (*9*). *Csf2*$^{-/-}$ mice displayed a partial reduction in intestinal MΦs, suggesting that MΦ development may, in part, depend on this growth factor (*9*). CSF2 has recently been shown to license the effector profile of MΦs in the inflamed brain, implicating an impact on MΦ function in addition to development (*21*). Whether these observations on CSF2 extend to MΦ development and function in the intestine remain unknown.

Here, we report a molecular and spatial framework governing cross-talk between host and microbiota that regulates MΦ

[1]Department of Immunology, University of Toronto, Toronto, ON, Canada. [2]Toronto General Hospital Research Institute, University Health Network, Toronto, ON, Canada. [3]Peter Munk Cardiac Centre, Ted Rogers Centre for Heart Research, Toronto, ON, Canada. [4]Institute of Physiology, University of Zürich, Zürich, Switzerland. [5]Institute of Biomedical Engineering, University of Toronto, Toronto, ON, Canada. [6]Department of Microbiology and Molecular Genetics, Oklahoma State University, Stillwater, OK, USA. [7]Graduate School of Biostudies, Kyoto University, Kyoto, Japan.
*Corresponding author. Email: arthur.mortha@utoronto.ca

heterogeneity. We identified SILTs as a critical niche for the developmental and functional programming of monocyte-derived SILT-associated MΦs (SAMs). Microbe-derived extracellular ATP ($ATP^{ex}$), acting through purinergic receptor P2X 7 (P2X7R)– and NLR family pyrin domain containing 3 (NLRP3)–expressing myeloid cells, drives CSF2 production by ILC3s to induce the developmental and functional transition of monocytes to SAMs along a differentiation pathway distinct from LP-associated MΦs (LAMs). CSF2-dependent SAMs mediated antimicrobial host protection, implicating SILTs as previously underappreciated, broadly scattered myeloid reservoirs across the gut. Collectively, our findings identify a molecular and spatial framework for the anatomically contained differentiation of intestinal MΦs, centered around a microbiota-fueled, ILC3-driven, and CSF2-dependent axis that integrates signals indicative of microbial energy into the developmental and functional heterogeneity of MΦs.

## RESULTS

### CSF2 maintains intestinal monocyte-derived MΦs

Tissue-resident MΦs in extraintestinal organs group into monocyte- or fetal-derived subpopulations based on cross-organ conserved expression of the following markers: the chemokine receptor CCR2, the phosphatidylserine receptor Tim-4, lymphatic vessel endothelial hyaluronan receptor 1 (LYVE1), and major histocompatibility complex 2 (MHCII) (*2*). In the gut, MΦs have been classified by Tim-4 and CD4 expression and the "monocyte waterfall" gating strategy, the latter tracking the transition of monocyte into MΦ using the markers Ly6C and MHCII (*4*, *22*). To determine the full scope of gut MΦ heterogeneity, we performed single-cell RNA sequencing (scRNA-seq) on CD11b-enriched cells isolated from the colonic LP of healthy adult mice (8 to 12 weeks old). Subsetting and re-analysis of the MΦ/monocyte clusters, identified based on their expression of *Csf1r*, *Cx3cr1*, and *C1qa* and the absence of dendritic cell (DC) markers, resulted in nine distinct clusters, revealing an anticipated heterogeneity within the colonic MΦ pool (Fig. 1A and fig. S1, A to D). MΦs in clusters 0 and 5 highly expressed *Lyve1*, *Mrc1*, *Maf*, and *Timd4* (Fig. 1, B and C) (*2*, *6*, *23*). MΦs in clusters 0 and 5 coexpressed *Cd4* but virtually no *Ccr2*. Cluster 4 was marked by high expression of *Ly6c2*, identifying them as monocytes, whereas cells in clusters 1 and 6 were annotated as monocyte-derived MΦs based on their high *Ccr2* expression (Fig. 1, B and C). *Lyz1* expression almost exclusively overlapped with *Il22ra2* expression in cluster 2, both genes previously reported to be also expressed in DCs located within small intestinal SILTs (*24*). Cluster 7 MΦs expressed *Retnla*, indicative of $RELM\alpha^+$ MΦs. Cluster 8 cells showed an unexpected expression of *Pecam1*, suggesting the existence of a MΦ population possibly involved in the interactions with endothelial or epithelial cells (Fig. 1, B and C). Multiparameter flow cytometry on colonic LP $CD64^+$ $CD11b^+$ cells recapitulated the distinct and partial overlap in the expression of Tim-4, CD4, CCR2, MHCII, and Ly6C across MΦs aligning with the previous classification into $Tim\text{-}4^+CD4^+$, $Tim\text{-}4^-CD4^+$, and $Tim\text{-}4^-CD4^-$ MΦs (Fig. 1D). Using flow cytometry, $Tim\text{-}4^-CD4^-$ MΦs were further delineated into $Ly6C^+$, $CCR2^+$, and $CCR2^-$ MΦs, suggesting a developmental relationship to monocytes and confirming the suitability of these markers for the analysis of colonic MΦs (Fig. 1D and fig. S1, E and F) (*2*, *4*).

Previous investigations into $Csf2^{-/-}$ mice did not use this detailed classification of MΦs, prompting us to revisit the requirements for CSF2 on gut MΦ heterogeneity (*9*). Comparing cluster relative abundance on scRNA-seq datasets generated from wild-type (WT) littermate controls and $Csf2^{-/-}$ mice indicated a reduction of MΦs within clusters 0, 2, 3, 5, 7, and 8 in the absence of *Csf2* (Fig. 1E). Analysis of MΦs in the colonic LP using flow cytometry confirmed the reduction in $Tim\text{-}4^-CD4^-$ MΦs and $Tim\text{-}4^-CD4^+$ MΦs in $Csf2^{-/-}$ mice. The same MΦ populations were similarly reduced in $Ccr2^{-/-}$ mice, implicating the developmental origin of these two MΦ subpopulations as monocyte derived (Fig. 1F and table S1). A decrease in both tissue-infiltrating $Ly6C^{hi}$ monocytes and $CCR2^+$ MΦs suggested a possible developmental blockade along the monocyte-to-MΦ transition in $Csf2^{-/-}$ mice (Fig. 1G and fig. S1G). In contrast to $Rag2^{-/-}$ mice injected with neutralizing anti-CSF2 antibodies, MΦs and monocytes from $Csf2^{-/-}$ and WT mice showed comparable levels of MHCII expression (fig. S1H) (*25*). In addition to the effects on monocytes and $CCR2^+$ MΦs, $Tim\text{-}4^+$ MΦs were partially affected in $Csf2^{-/-}$ mice, suggesting that all MΦ subpopulations variably depend on this growth factor (Fig. 1E).

### Monocytes and $Tim\text{-}4^-CD4^-$ MΦs are developmentally related

$Tim\text{-}4^+$ MΦs are a long-lived, fetal-derived population with minimal replacement by monocytes. It has been proposed that the expression of Tim-4 may reflect long-term residency within a tissue after differentiation (*4*, *6*, *26*–*28*). To determine the long-term MΦ turnover by infiltrating monocytes, we performed parabiosis of CD45.1 C57BL/6 and CD45.2 $Ccr2^{-/-}$ mice to assess the chimerism of each MΦ subpopulation after 6 or 12 months. As expected, CD45.2 $Ccr2^{-/-}$ parabionts showed CD45.1 frequencies comparable to blood monocytes in both the colonic $Tim\text{-}4^-CD4^-$ and $Tim\text{-}4^-CD4^+$ MΦ compartments (fig. S1, I and J), consistent with their continual replacement by blood monocytes. Unexpectedly, $Tim\text{-}4^+$ MΦs were also replaced by donor CD45.1 monocytes, albeit at a slower rate, suggesting a homeostatic contribution of monocytes to the maintenance of $Tim\text{-}4^+$ MΦs (fig. S1, I and J).

To confirm these results, we used a tamoxifen-inducible fate-mapping model. Tamoxifen-containing chow was provided to $Ccr2^{CreERT2}$ x *Rosa26*-LSL-tdTomato ($Rosa26^{td}$) mice during a 1-week pulse phase, followed by a chase period with normal chow for either 1 or 52 week(s). Loss of Tomato labeling was measured in each MΦ subpopulation to assess the replacement of MΦs by newly infiltrated monocytes. Tamoxifen administration labeled ~94% of all blood $Ly6C^{hi}$ monocytes within the 1-week pulse phase, whereas the induced Tomato label was completely lost in monocytes by 52 weeks (fig. S1K). Colonic $Ly6C^{hi}$ monocytes and $Tim\text{-}4^-CD4^-$ MΦs showed labeling efficiency similar to blood monocytes, whereas $Tim\text{-}4^-CD4^+$ MΦs displayed partial Tomato labeling (64%). Unexpectedly, ~17% of all $Tim\text{-}4^+$ MΦs were labeled after the 1-week pulse phase, suggesting either a possible contribution of monocytes to this population during tamoxifen administration or low *Ccr2* expression levels and recombinase activity within a subset of $Tim\text{-}4^+$ MΦs (fig. S1K). After the first 7 days of the chase period, $Tim\text{-}4^-CD4^-$ MΦs (containing $Ly6C^+$ and $CCR2^+$ cells) displayed replacement by bone marrow–derived (BM) monocytes, as indicated by the loss of Tomato labeling (fig. S1K). $Tim\text{-}4^-CD4^+$ MΦs and $Tim\text{-}4^+$ MΦs did not show signs of replacement,

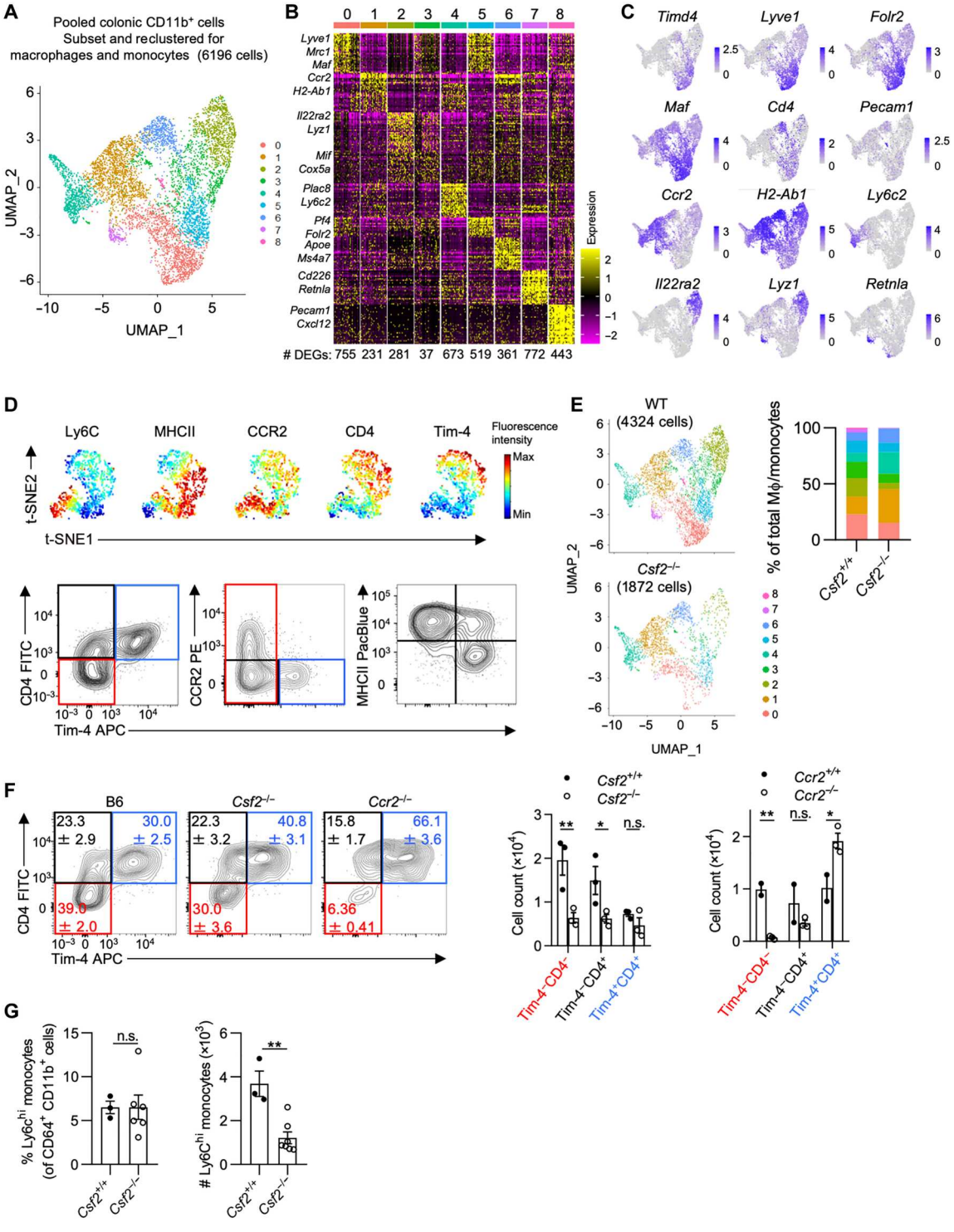


**Fig. 1. Developmental requirements and kinetics of colonic LP MΦs.** (**A**) UMAP projection of the combined analysis of WT and *Csf2*$^{-/-}$ datasets subsetted and reclustered for MΦs and monocytes visualized together. (**B**) Heatmap depicting the top 30 DEGs for each cluster ($log_2$FC threshold = 0.25, min.pct = 0.25, adjusted $P < 0.05$), downsampled to 50 cells for visualization. The number of DEGs in each cluster is shown. (**C**) Feature plots illustrating expression of subset-defining genes. (**D**) Representative flow cytometry analysis using (top) unbiased t-distributed stochastic neighbor embedding (t-SNE) dimensionality reduction of colonic CD64$^+$ CD11b$^+$ cells showing expression of common MΦ markers or (bottom) Tim-4/CD4, Tim-4/CCR2, and Tim-4/MHCII classification strategies. (**E**) UMAP projection (left) of MΦs/monocytes in WT versus *Csf2*$^{-/-}$ colon with relative abundance of each cluster (right). (**F**) Contour plots (left) and quantification (right) of colonic MΦs in B6, *Csf2*$^{-/-}$, and *Ccr2*$^{-/-}$ mice. (**G**) Percentage and absolute counts of Ly6C$^{hi}$ monocytes in WT and *Csf2*$^{-/-}$ mice. Data shown in (A) to (C) and (E) are from the same scRNA-seq experiment obtained from cells pooled from at least three animals per genotype. Two-way analysis of variance (ANOVA) with post hoc Šidák's multiple comparisons test (F) or unpaired Student's *t* test (G) was performed. FITC, fluorescein isothiocyanate; PE, phycoerythrin; APC, allophycocyanin; n.s., not significant.

suggesting a slower replacement rate in line with our parabiosis experiments (fig. S1, I to K). After the 52-week chase period, all MΦ subpopulations lost the Tomato label (fig. S1K). These results indicate that all colonic MΦs share a monocytic origin, with Tim-4$^-$CD4$^-$ MΦs showing the fastest replacement and strongest reliance on CSF2 (Fig. 1F and fig. S1G).

### Diversified microbiotas promote the accumulation of Tim-4$^-$CD4$^-$ MΦs

Tissue-resident Tim-4$^+$ MΦs dominate the MΦ pool during embryogenesis and are found in all tissues at early time points of fetal development, whereas Tim-4$^-$ MΦs postnatally arise from BM monocytes (*2*). In the gut, this development requires the microbiota (*4*, *22*). Our fate-mapping and parabiosis data show that colonic MΦ subpopulations display different rates of monocyte replacement, suggesting distinct appearances of the MΦ subpopulations in the neonatal and adult intestine. To delineate the developmental kinetics of MΦs, we assessed the composition of MΦs starting in the neonatal colon, tracking along the first weeks of life until adulthood. In line with previous reports, embryonically derived Tim-4$^+$CD4$^+$ MΦs primarily comprise the colons of newborn mice, followed by increased abundance of Tim-4$^-$CD4$^-$ MΦs at 3 to 4 weeks of age. This time corresponds to weaning and the establishment of a diversified microbiota (Fig. 2A) (*29*). By 8 to 12 weeks after birth, Tim-4$^-$CD4$^-$ MΦs comprise the majority of colonic MΦs, suggesting a microbiota-driven adaptation of the MΦ pool. These adaptations in gut MΦs mirror previously reported observations of intestinal CSF2 production, which similarly increased until week 8 in a microbiota-dependent fashion (*9*).

Depletion of the microbiota using broad-spectrum antibiotics in adult mice shifted the MΦ pool in favor of Tim-4$^+$CD4$^+$ MΦs, confirming a requirement of the microbiota in regulating gut MΦ composition (Fig. 2B). In contrast, reconstituting germ-free (GF) mice with an adult specific pathogen–free (SPF) microbiota increased Tim-4$^-$CD4$^-$ MΦs at the expense of Tim-4$^+$CD4$^+$ MΦs (Fig. 2C). Colonization of adult SPF mice with the protozoan commensal *T. mu* further increased the abundance of Tim-4$^-$CD4$^-$ MΦs (fig. S2A). A comparable shift toward Tim-4$^-$CD4$^-$ MΦs was also observed when analyzing "rewilded" mice, i.e., ex-SPF mice that were colonized with the microbiota found in pet store mice (fig S2B). These findings suggest that the increase in Tim-4$^-$CD4$^-$ MΦs in the colon may be due to an increase in microbiota-driven monocyte replacement.

To track the rate of monocyte replacement, we labeled all *Cx3cr1*-expressing cells in tamoxifen-inducible *Cx3cr1*$^{CreERT2}$ x *Rosa26*$^{tdTomato}$ mice and followed the loss of tdTomato labeling in each MΦ population after colonization with *T. mu* (fig. S2C). Compared with uncolonized littermate controls, *T. mu*–colonized mice showed reduced percentages of tdTomato$^+$ cells particularly in Tim-4$^-$CD4$^-$ MΦs, suggesting an increased replacement of these cells by tdTomato$^-$ monocytes (fig. S2D). Monocyte replacement was also elevated in Tim-4$^-$CD4$^+$ MΦs and Tim-4$^+$CD4$^+$ MΦs. Collectively, our data demonstrate that diversifying the gut microbiota promotes MΦ replacement by monocytes and the accumulation of Tim-4$^-$CD4$^-$ MΦs. Colonization with *T. mu* has previously been found to increase the production of CSF2 by intestinal ILC3s, implicating a role for ILC3s in the elevated MΦ replacement rates (*30*). *Csf2*$^{-/-}$ mice treated with broad-spectrum antibiotics did not show alterations in Tim-4$^-$CD4$^-$ MΦs, suggesting that microbiota-driven changes in the colonic MΦ pool require CSF2 (Fig. 2D).

### CSF2-producing ILC3s support intestinal CCR2$^+$ Tim-4$^-$CD4$^-$ MΦs

Microenvironmental cues within anatomical niches are critical for imprinting tissue-resident MΦ identity in various organs (*31*). However, less focus has been placed on niches for monocyte-derived MΦs. In the gut, CSF2-producing ILC3s are abundantly found within postnatally formed SILTs (*9*). *Csf2*$^{tdTomato}$ reporter mice revealed an accumulation of tdTomato$^+$ cells within SILTs, prompting us to determine whether CSF2-producing ILC3s constitute supporting cells for monocyte-derived MΦs (Fig. 3A) (*9*). Quantification of CX3CR1$^+$CCR2$^+$ MΦs in the colonic LP or SILTs of *Cx3cr1*$^{+/EGFP}$*Ccr2*$^{+/RFP}$ mice uncovered an accumulation of monocyte-derived CCR2$^+$ MΦs around SILTs compared with the surrounding LP (Fig. 3, B and C). SILTs contain B cells, ILC3s, and T cells, the latter two being possible sources of CSF2 in the LP (*9*, *32*). We compared CSF2 production by T cells and ILC3s within SILTs or the surrounding LP by intracellular cytokine staining. T cells and ILC3s contributed equally to the pool of spontaneous CSF2 within the LP, but ILC3s constituted the predominant source of CSF2 within SILTs (Fig. 3, D and E). To confirm the role of ILC3s as a source for CSF2, we analyzed the colonic MΦ composition across WT, *Rag2*$^{-/-}$, *Rorc*$^{Cre}$ × *Csf2*$^{fl/fl}$, *Rorc*$^{-/-}$, *Csf2*$^{-/-}$, *Vav1*$^{Cre}$ × *Csf2*$^{fl/fl}$, and *Rag2*$^{-/-}$*Il2rg*$^{-/-}$ mice. Only *Rag2*$^{-/-}$*Il2rg*$^{-/-}$ mice (lacking all lymphocytes), but not *Rag2*$^{-/-}$ mice (sufficient in ILCs), displayed a reduction in Tim-4$^-$CD4$^-$ MΦs, comparable to the decrease observed in *Csf2*$^{-/-}$ or *Rorc*$^{-/-}$ mice (lacking ILC3s and *Rorc*-expressing T cell subsets). Animals lacking *Csf2* in *Rorc*-expressing ILC3s and T cells (*Rorc*$^{Cre}$ × *Csf2*$^{fl/fl}$) or all hematopoietic cells (*Vav1*$^{Cre}$ × *Csf2*$^{fl/fl}$) recapitulated the altered MΦ composition found in both total body *Csf2*$^{-/-}$ and *Rorc*$^{-/-}$ mice but did not reach alterations observed in *Rag2*$^{-/-}$*Il2rg*$^{-/-}$ mice. This indicates that ILC3s, rather than T or B cells, regulate the homeostatic CSF2-dependent MΦ composition in the colon, possibly supplemented by CSF2-producing ILC1s, ILC2s, or natural killer cells in the absence of RAR-related orphan receptor gamma t (RORγt) (Fig. 3F).

To further validate the contribution of ILC3s to the regulation of colonic MΦs, we adoptively transferred $10^4$ fluorescence-activated cell sorting (FACS)–purified *Rorc*$^{+/EGFP}$ ILC3s from WT (ILC3$^{CSF2}$) or *Csf2*$^{-/-}$ (ILC3$^{\Delta CSF2}$) mice into *Rag2*$^{-/-}$*Il2rg*$^{-/-}$ recipients. We observed accumulation of Tim-4$^-$CD4$^-$ MΦs in the colonic LP after 6 weeks, indicating the dependency of Tim-4$^-$CD4$^-$ MΦs on ILC3-derived CSF2 (Fig. 3G and fig. S3, A, and B). Numbers of Tim-4$^-$CD4$^+$ and Tim-4$^+$CD4$^+$ MΦs were also slightly increased in *Rag2*$^{-/-}$*Il2rg*$^{-/-}$ mice after transfer of ILC3$^{CSF2}$, suggesting their partial dependency on CSF2-producing ILC3s (Fig. 3G). These findings demonstrate that CCR2$^+$ MΦs accumulate around colonic SILTs rich in CSF2-producing ILC3s that support Tim-4$^-$CD4$^-$ MΦ development (Fig. 3H).

CSF2 expression by ILC3s has previously been demonstrated to require an intact microbiota and the production of IL-1β (*9*). We observed a microbiota-dependent increase in monocyte-derived MΦs in the context of microbiotas complexified with nonbacterial commensals and, conversely, a decrease in the absence or strong reduction of gut commensal microbes (Fig. 2, A to G). These observations argue in favor of a conserved mechanism that integrates the

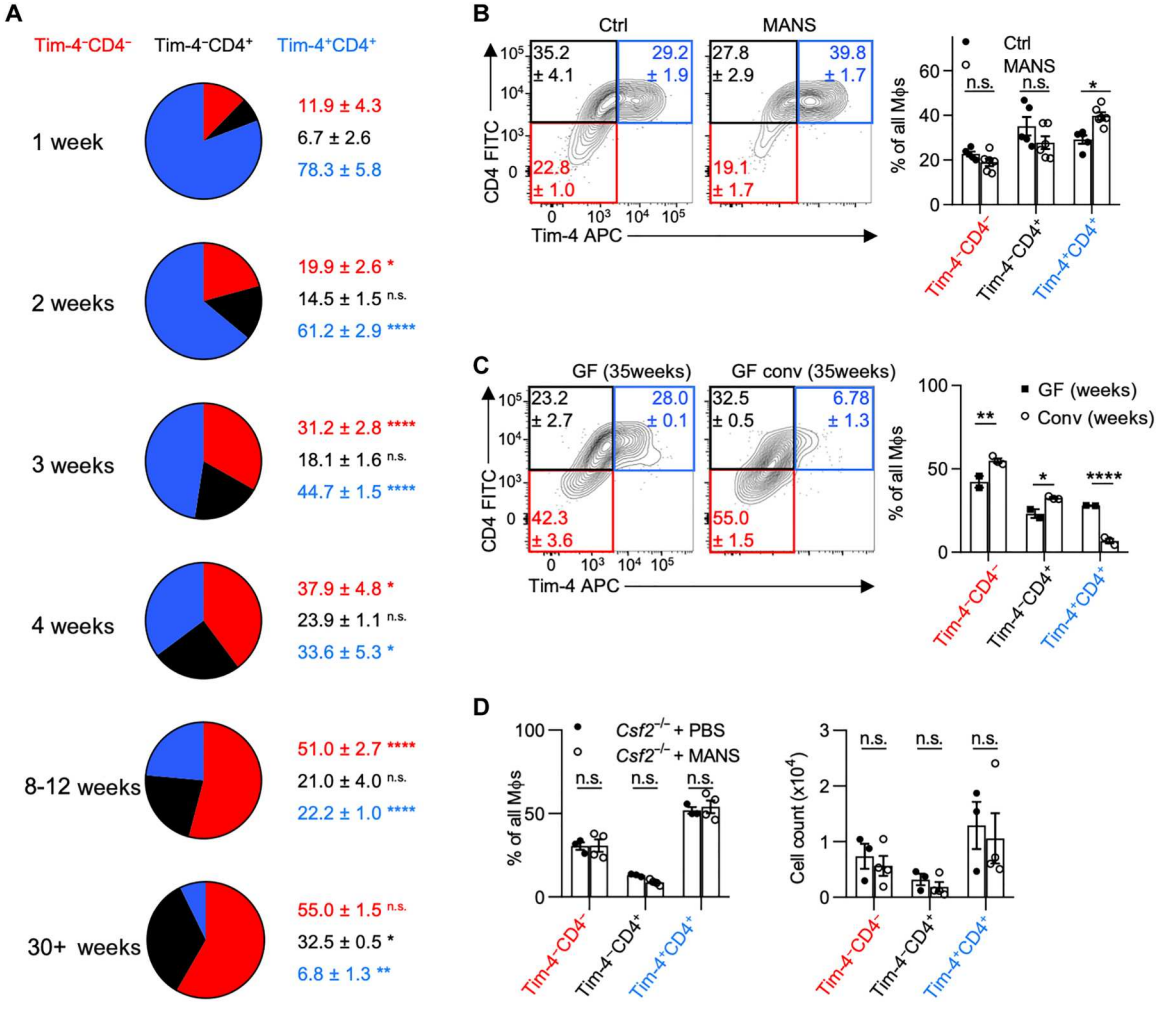


**Fig. 2. The development of colonic Tim-4⁻CD4⁻ MΦs requires an intact and diversified microbiota.** Colonic MΦ composition in (**A**) B6 mice across various ages, (**B**) B6 mice either left untreated or treated with broad-spectrum antibiotics [metronidazole, ampicillin, neomycin, streptomycin (MANS)], and (**C**) GF mice or GF mice conventionalized with SPF microbiota. (**D**) Colonic MΦ composition (left) and absolute counts of MΦ populations (right) in *Csf2*$^{-/-}$ mice either left untreated or treated with MANS for 2 weeks. Multiple unpaired *t* tests with two-stage Benjamini, Krieger, and Yekutieli false discovery rate test were performed for (A), $Q = 5\%$, reporting *q* values; each time point compared with previous time point. Two-way ANOVA with post hoc Šidák's multiple comparisons test was performed for (B) to (D). PBS, phosphate-buffered saline.

diversification of the microbiota into CSF2-dependent regulation of colonic MΦs.

## Microbial ATP$^{ex}$ regulates MΦ composition and CSF2 production

Diversification of the microbiota generates multiple new features within the microbial community, including adaptations to nutrients and synthesis of different metabolites (*33*). Such changes may not apply to individual microbial species but rather reflect a feature of complex community interactions (*34*). This raises the possibility for a conserved ubiquitously produced metabolite across all living microbes that indicates microbial vitality but, at the same time, serves as a molecular motif for immune recognition and activation that can indirectly affect MΦ homeostasis. ATP is one such metabolite capable of promoting intestinal immunity (*35*). We recently demonstrated that colonization with the protozoan commensal *T. mu* induces immune activation in the colon, including increased monocyte infiltration, regulated by elevated intestinal ATP$^{ex}$ levels and inflammasome activation (*14*). ATP$^{ex}$ is a common danger-associated molecular pattern that correlates with the presence of the microbiota and subsequently regulates local adaptive immune cells through P2X7R-dependent recognition by CD11c$^{+}$ myeloid cells (*35*, *36*). Thus, we asked whether ATP$^{ex}$ might serve as a rheostatic indicator of the microbiota, capable of regulating colonic MΦ composition.

In line with previous studies, we first confirmed that ATP$^{ex}$ levels in the gut lumen corresponded to microbiota abundance by comparing fecal ATP$^{ex}$ in SPF, antibiotics-treated, and germ-free mice (fig. S4A). ATP was shown to be released by multiple bacterial species through an unknown mechanism while undergoing cellular respiration during the growth phase in vitro (*37*). To specifically investigate the role of bacteria-derived ATP, we used a mutant strain of commensal *Escherichia coli* MG1655 lacking the operons encoding the ATP synthase subunits A-G [Δ(*atpA-atpG*)] (*38*). In contrast

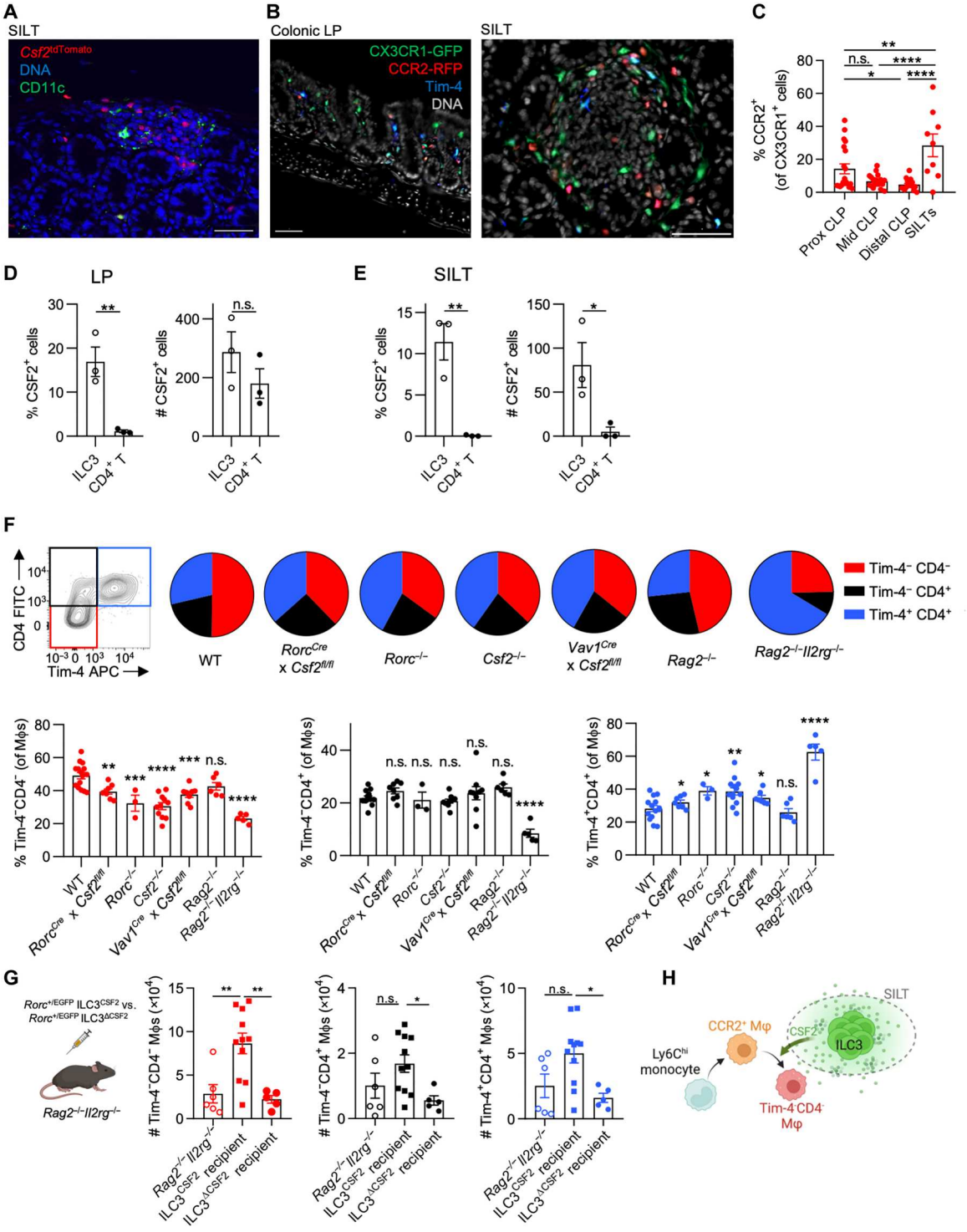


**Fig. 3. CSF2-producing ILC3s in SILTs induce CCR2$^+$ Tim-4$^-$CD4$^-$ MΦs.** (**A**) Representative immunofluorescence image of a colonic SILT of *Csf2*$^{tdTomato}$ mouse stained for CD11c and DNA [4′,6-diamidino-2-phenylindole (DAPI)]. (**B**) Representative immunofluorescence images of colonic LP and SILT of *Cx3cr1*$^{+/GFP}$ *Ccr2*$^{+/RFP}$ mice stained for Tim-4 and DNA. Scale bars, 50 μm (A and B). (**C**) Proportion of CCR2-RFP$^+$ of CX3CR1-GFP$^+$ cells based on CellProfiler quantification of images in each colonic LP (CLP) region and SILTs, as indicated. (**D** and **E**) Percentage and absolute counts of CSF2$^+$ ILC3s and CD4$^+$ T cells (D) in colonic LP and (C) within SILTs. (**F**) Colonic MΦ composition as indicated. (**G**) A total of $10^4$ FACS-sorted small intestinal *Rorc*$^{+/EGFP}$ ILC3s from either WT or *Csf2*$^{-/-}$ mice were adoptively transferred into *Rag2*$^{-/-}$*Il2rg*$^{-/-}$ mice, and recipients were analyzed at 6 weeks (left). Quantifications (right) of colonic MΦ populations after transfer, as indicated. (**H**) Schematic overview of how SILT-enriched, CSF2-producing ILC3s affect MΦ development. One-way ANOVA with post hoc Tukey's test (C and G), unpaired Student's *t* test (D and E), or one-way ANOVA with Dunnett's test compared with WT (F) was performed.

to WT *E. coli* or a mutant lacking nitrate reductase genes [Δ*narG* Δ*narZ* Δ(*napD-napA*)], the adenosine triphosphatase (ATPase)–deficient mutant was unable to secrete ATP during growth in vitro, confirming an ATPase-dependent increase in $ATP^{ex}$ (fig. S4, B and C). Transformation of the Förster resonance energy transfer–type ATP biosensor ATeam 3.10 into these *E. coli* strains enabled the quantification of intracellular ATP ($ATP^{int}$) levels (fig. S4D) (*39*). Accordingly, less pronounced $ATP^{int}$ levels were observed in the ATPase-deficient *E. coli* in vitro, confirming its metabolic impairment and release of ATP (fig. S4, E and F).

To determine whether impaired ATP metabolism in commensals affects MΦ heterogeneity in the gut, GF mice were monocolonized with control *E. coli*, Δ(*atpA-atpG*) *E. coli*, or Δ(*atpA-atpG*) *E. coli* supplemented with the ATP derivative γS-ATP (ATPγS) via daily rectal enemas. Untreated groups received daily enemas of sterile phosphate-buffered saline (PBS). Colonic MΦ composition was assessed 7 days after engraftment to avoid confounding effects of adaptive immune cells on the colonizing microbes (*40*, *41*). Despite equal colonization, Δ(*atpA-atpG*) *E. coli* produced less $ATP^{int}$ at the time of analysis compared with the WT strain (fig. S4, G and H). Both *E. coli* strains displayed equal and preferred localization in the lumen of the gut with minimal mucosal localization (fig. S4, I and J). Nevertheless, mice colonized with control *E. coli* showed higher infiltration of $Ly6C^+$ and $CCR2^+$ MΦs in comparison with Δ(*atpA-atpG*) *E. coli*–colonized mice (Fig. 4, A and B). Application of rectal ATPγS in GF mice colonized with Δ(*atpA-atpG*) *E. coli* recapitulated the increase in $Ly6C^+$ monocytes and $CCR2^+$ MΦs, demonstrating the requirement of bacterial-derived $ATP^{ex}$ as a driver of monocyte infiltration and MΦ differentiation (Fig. 4, A and B). No impact was observed on other MΦ subsets, although it is possible that these may manifest after a longer time of colonization, given their slower turnover rates from monocytes (fig. S4K). CSF2 governed the abundance of $CCR2^+$ MΦs and has previously been reported to be produced by ILC3s in a microbiota-dependent manner (*9*, *42*). To determine the impact of $ATP^{ex}$ on ILC3s, we also analyzed CSF2 production and ILC3 counts in the colonic LP. Mice gavaged with either WT *E. coli* or Δ(*atpA-atpG*) supplemented with ATPγS showed an increase in ILC3 numbers and $CSF2^+$ ILC3s when compared with untreated GF mice or GF mice colonized with Δ(*atpA-atpG*) *E. coli* (Fig. 4C). These findings implicate the regulation of CSF2-producing ILC3s by microbe-derived $ATP^{ex}$ and led us to investigate how $ATP^{ex}$ may activate ILC3s.

## $ATP^{ex}$ activates purinergic receptors on myeloid cells to promote ILC3-derived CSF2

Colonization of the gut by commensal microbes induces the release of IL-1β by MΦs (*43*). $ATP^{ex}$ engages P2X7R, which can activate NLRP3 to result in the processing of pro–IL-1β release of bioactive IL-1β (*44*). To identify cells that could respond to $ATP^{ex}$ stimulation, we analyzed P2X7R expression on colonic lymphoid and myeloid cells and found that MΦs expressed the highest levels of P2X7R (fig. S4, L to N). P2X7R expression on ILC3s was extremely low (fig. S4N). At the subpopulation level, $Tim\text{-}4^+$ and $Tim\text{-}4^-CD4^+$ MΦs expressed the highest levels of P2X7R. We confirmed that P2X7R staining levels were not an artifact of MΦ autofluorescence, because fluorescence was not detected in $P2rx7^{-/-}$ MΦs (Fig. 4D). A higher proportion of $Tim\text{-}4^+$ MΦs coexpressed pro–IL-1β protein compared with $Tim\text{-}4^-CD4^-$ and $Tim\text{-}4^-CD4^+$ MΦs despite lower mRNA *Il1b* transcripts (Fig. 4E and fig. S4P). We then determined whether colonic MΦs expressed *Nlrp3* and found low but detectable expression across all MΦ subpopulations, including fetal-derived $Tim\text{-}4^+$ MΦs (Fig. 4F). DCs expressed *Nlrp3*, *P2rx7*, and *Il1b* but showed lower P2X7R protein levels across all subsets when compared with colonic MΦs (fig. S4, M and O). Therefore, MΦs, most likely $Tim\text{-}4^+$ MΦs, rather than DCs or monocytes contribute to steady-state P2X7R-mediated $ATP^{ex}$ sensing. These findings also complement previous reports showing that MΦ depletion in the steady state alters microbiota-dependent, IL-1β-driven CSF2 production by ILC3s (*9*, *25*).

To determine whether the absence of *Nlrp3* affects the colonic composition of MΦs, we analyzed MΦ subsets in $Nlrp3^{-/-}$ mice and their littermate controls and observed a decrease in $Tim\text{-}4^-CD4^-$ MΦ numbers (Fig. 4G). In line with a decrease in CSF2-dependent MΦs in these mice, $Nlrp3^{-/-}$ and $P2rx7^{-/-}$ mice showed a reduction in ILC3-derived CSF2 (Fig. 4, H and I). Monocyte-derived $CCR2^+$ MΦs and $Tim\text{-}4^-CD4^-$ MΦs were decreased within SILTs of $Nlrp3^{-/-}$ mice (Fig. 4J). To determine whether ILC3s could directly sense and respond to $ATP^{ex}$ via CSF2 production despite their low P2X7R levels, we stimulated ILC3s from WT, $P2rx7^{-/-}$, or $Nlrp3^{-/-}$ mice with either ATPγS or IL-1β. Although IL-1β expectedly increased CSF2-producing ILC3s, stimulation with ATPγS failed to activate ILC3s (Fig. 4K). This demonstrates that ILC3-derived CSF2 production requires NLRP3 and P2X7R expression, likely by MΦs or DCs (Fig. 4L). Together, these data indicate that microbe-derived $ATP^{ex}$ regulates colonic monocyte-derived MΦs via P2X7R-dependent NLRP3-mediated IL-1β activation in myeloid cells to induce CSF2 production by ILC3s.

## scRNA-seq reveals unique SAM populations

The analysis of MΦ populations in $Nlrp3^{-/-}$ mice suggested differential regional effects on MΦs within LP and SILTs. To incorporate spatial information into the actions of CSF2 on colonic MΦs at higher granularity, we performed scRNA-seq analysis of MΦs isolated from either SILTs or LP of WT or $Csf2^{-/-}$ mice. Live $Cx3cr1^{+/EGFP}Ccr2^{+/RFP}$ colonic tissues enabled visual demarcation of SILTs and LP using a fluorescent stereomicroscope (Fig. 5A). Biopsy punches containing colonic SILTs or SILT-free LP were isolated and digested before enrichment for $CD11b^+$ cells by magnetic beads (>90% purity) and subsequent scRNA-seq analysis (Fig. 5A). Uniform Manifold Approximation and Projection (UMAP) dimensionality reduction and combined analysis of all four groups ($LP^{WT}$, $SILT^{WT}$, $LP^{Csf2-/-}$, and $SILT^{Csf2-/-}$) followed by subsetting and reanalysis of the MΦ/monocyte populations, based on parameters previously detailed, resulted in nine distinct clusters as seen before (Figs. 1A and 5B). Cells within clusters 0, 1, and 7 were enriched in the LP, whereas SILTs primarily comprised clusters 2, 3, 5, and 6, indicating preferential localization of some MΦ subpopulations within SILTs (Fig. 5B). Annotation of the nine clusters based on their differentially expressed genes (DEGs) prompted us to label MΦ clusters 0 and 5, which highly expressed *Lyve1*, *Mrc1*, *Maf*, and *Timd4*, as $Tim\text{-}4^+$ LAMs and $Tim\text{-}4^+$ SAMs, respectively. We also identified clusters corresponding to $CCR2^+$ MΦs (cluster 1), monocytes (cluster 4), $Tim\text{-}4^-CD4^+$ MΦs (cluster 6), $RELMα^+$ MΦs (cluster 7), and epithelium/endothelium-associated $Pecam1^+$ MΦs (cluster 8) (Fig. 1B and fig. S5A). Although previous reports identified $Tim\text{-}4^-CD4^+$ MΦs and investigated their developmental kinetics, the functions of this subpopulation remain unclear (*4*).

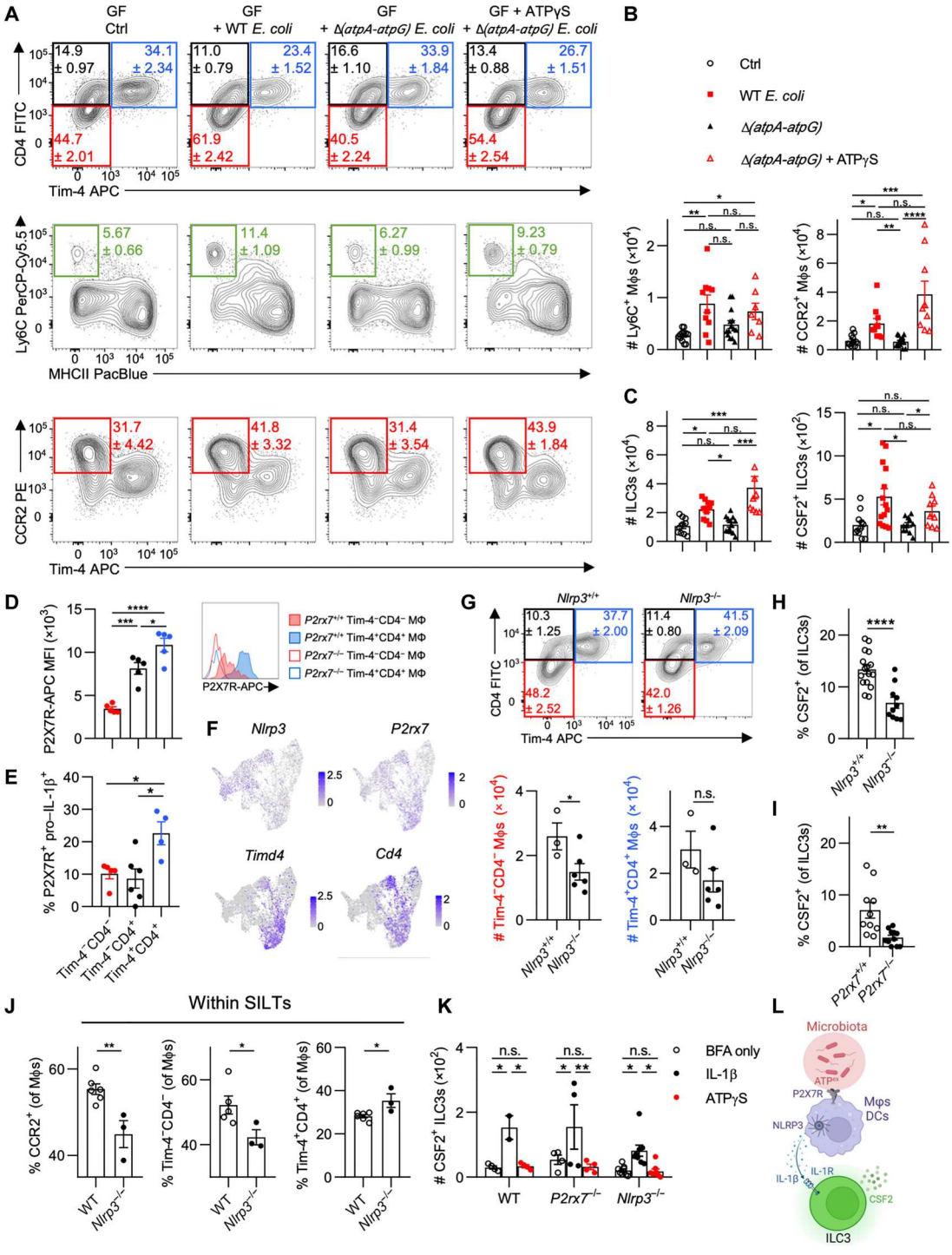


**Fig. 4. Microbial ATP regulates MΦ composition and drives CSF2 production by ILC3s through P2X7R and NLRP3 inflammasome signaling.** (A to C) GF mice were orally gavaged with WT or Δ(*atpA-atpG*) *Strr E. coli* MG1655, with a group of Δ(*atpA-atpG*) *Strr E. coli* MG1655 recipients receiving daily intrarectal applications of ATPγS. Mice were analyzed 1 week later. (**A**) Representative flow cytometry plots show colonic monocyte and MΦ composition. (**B**) Quantifications of Ly6C$^+$ and CCR2$^+$ MΦs. (**C**) Quantifications of total ILC3s and CSF2-producing ILC3s in the colon. (**D** and **E**) Each WT colonic MΦ population was assessed for (D) median fluorescence intensity (MFI) of P2X7R staining, with histograms (right) showing staining in *P2rx7*$^{+/+}$ versus *P2rx7*$^{-/-}$ mice, or (E) percentage of P2X7R$^+$ pro–IL-1β$^+$ cells. (**F**) Feature plots illustrating expression of indicated genes in colonic MΦs/monocytes. (**G**) Contour plots (top) and quantification (bottom) of colonic MΦs in B6 and *Nlrp3*$^{-/-}$ littermates. (**H** and **I**) Percentage of CSF2-producing colonic ILC3s in *Nlrp3*$^{-/-}$ and *P2rx7*$^{-/-}$ mice with respective littermate controls. (**J**) WT and *Nlrp3*$^{-/-}$ colonic SILTs were isolated and assessed for percentage of each MΦ population. (**K**) Colonic LP leukocytes were treated with vehicle control, IL-1β, or ATPγS in the presence of brefeldin A (BFA) and quantified for CSF2$^+$ ILC3s. (**L**) Schematic overview of how microbiota-derived ATP$^{ex}$ regulates ILC3-derived CSF2. For (J), each data point represents pooled SILTs from two or three mice. One-way ANOVA with post hoc Tukey's test (B to E), two-way ANOVA with post hoc Šidák's multiple comparisons test (K), or unpaired Student's *t* test (G to J) was performed.

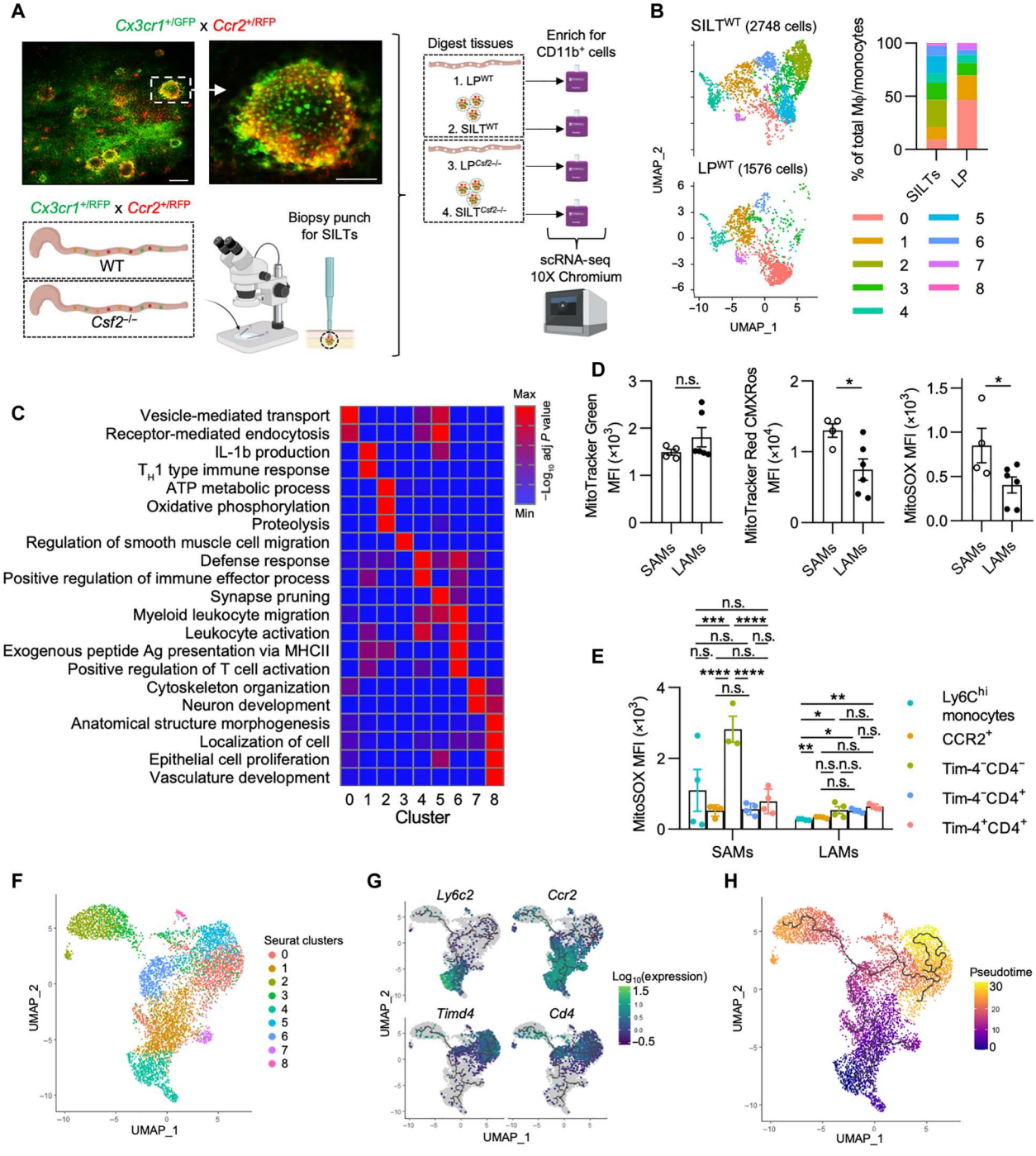


**Fig. 5. scRNA-seq analysis of colonic LP MΦs inside and outside SILTs predicts their different functions based on localization.** (**A**) Representative live images [scale bars, 200 μm (left) and 100 μm (right)] of a colonic SILT in *Cx3cr1*$^{+/GFP}$ *Ccr2*$^{+/RFP}$ mice and experimental scheme for scRNA-seq setup. Data are subsetted and reclustered for MΦs and monocytes as in Fig. 1A. (**B**) UMAP projection of MΦs/monocytes of SILT$^{WT}$ and LP$^{WT}$ (left) with quantification of the relative cluster abundance for each sample (right). (**C**) Pathway enrichment analysis (gProfiler, GO biological processes) using DEGs for each cluster (from Fig. 1B). (D and E) Colonic SAMs and LAMs were isolated, stained with mitochondrial dyes, and assessed for staining MFI as indicated. $T_H1$, T helper 1. (**D**) MFIs of mitochondrial dyes in total SAMs and LAMs. (**E**) MitoSOX MFI of each MΦ population in each colonic region. (**F**) UMAP dimensionality reduction using Monocle 3 was performed and visualized with overlaid Seurat annotations from Fig. 1A. (G and H) Trajectory analysis was performed using Monocle 3 as indicated by solid black lines. (**G**) Changes in expression of subset-defining genes were visualized in conjunction with trajectory analysis. (**H**) Pseudotime analysis was performed and visualized using Monocle 3. Unpaired Student's *t* test (D) or one-way ANOVA with post hoc Tukey's test (E) was performed.

Cluster 6 MΦs, corresponding to Tim-4$^-$CD4$^+$ MΦs, displayed a gene expression pattern similar to that reported in inflammatory microglia and border-associated MΦs, including the expression of *Apoe*, *Ms4a7*, and *Tmem119* (*6*, *21*, *45*, *46*). Biological pathways enrichment analysis on MΦ cluster 6 indicated that Tim-4$^-$CD4$^+$ MΦs are involved in leukocyte activation, antigen presentation, and T cell activation, suggesting a proinflammatory role for this subpopulation (Fig. 5C).

Cluster 2 and 3 MΦs were found almost exclusively in SILTS and expressed high levels of *Il22ra2* and *Lyz1*, markers reported for SILT-residing CD11c$^+$MHCII$^+$CD11b$^-$CD103$^-$ DCs in the small intestine (*24*). However, MΦ identity for cluster 2 and 3 cells was confirmed by their expression of MΦ markers (*Csf1r*, *Cx3cr1*, *C1qa*, *Adgre1*, and *Fcgr1*) and the absence of DC markers (*Flt3*, *Dpp4*, and *Zbtb46*) (fig. S1, B to D). The absence of *Timd4* and *Cd4* expression and the low level of *Ccr2* expression in cluster 2 and 3 MΦs suggest that these cells correspond to a subset of the Tim-4$^-$CD4$^-$ MΦs (Fig. 1B). Cluster 2 and 3 SAMs were enriched in ATP metabolism, oxidative phosphorylation (OXPHOS), and phagocytic pathways, indicative of a population high in energy demand and possibly involved in antimicrobial host defense (Fig. 5C). This prompted us to characterize mitochondria, as a major bioenergetic organelle, in LAMs and SAMs. Comparing mitochondrial mass (MitoTracker Green), mitochondrial membrane potential (MitoTracker Red) as an indicator of energy metabolism, and the production of reactive oxygen species (ROS) particularly superoxide (SOX) (MitoSOX) in LAMs and SAMs, we found equal mitochondrial numbers in MΦs across LP and SILTs but higher mitochondrial membrane potential and ROS production in SAMs (Fig. 5D). Tim-4$^+$ MΦs had higher numbers of mitochondria compared with all other MΦ subpopulations, as previously reported (*47*), regardless of colonic localization (fig. S5B). The higher MitoSOX staining in SAMs was attributed to a greater staining in Ly6C$^+$ monocytes and especially Tim-4$^-$CD4$^-$ SAMs, in line with the pathway analysis of the scRNA-seq data (Fig. 5, C and E).

Considering these notable differences between LAM and SAM populations, we sought to determine the developmental relationship between each MΦ cluster from our scRNA-seq data and thus performed trajectory analysis using Monocle 3 with Seurat-generated clusters overlaid (Fig. 5F). This analysis predicted a common origin for all LAMs and SAMs within the monocyte cluster 4, supporting our fate-mapping and parabiosis studies (Fig. 5G and fig. S1, I to K). Pseudotime analysis revealed a gradual loss of *Ly6c2* and *Ccr2* expression and gain of *Cd4* and *Timd4* expression as cells transitioned from monocytes toward differentiated MΦs (Fig. 5G). Tim-4$^-$CD4$^+$ MΦs represent a differentiation branching point, at which cells transition either into Tim-4$^+$ MΦs (clusters 0 and 5) or into SAMs (first to cluster 3 and then cluster 2) (Fig. 5, F to H). Given that Tim-4$^-$CD4$^+$ MΦs were least affected by perturbations in the microbiota (Fig. 2, A to E), their status as a defining branch point for tissue-resident MΦs may be worth additional investigation in the future. In summary, our scRNA-seq analyses reveal a previously undescribed SILT-associated Tim-4$^-$CD4$^-$ MΦ population, high in energy metabolism and ROS production, possibly originating from Tim-4$^-$CD4$^+$ MΦs along a distinct differentiation pathway and within a distinct anatomic location.

### CSF2 is a spatial determinant of MΦ development and function in the gut

To determine whether LAMs and SAMs are differentially regulated by CSF2, we first identified MΦ clusters that are most likely to be CSF2 responsive based on their *Csf2ra* and *Csf2rb* expression (Fig. 6A). All MΦ clusters except for *Timd4*$^+$*Lyve1*$^+$ MΦs (clusters 0, 5, and 8) expressed detectable levels of *Csf2ra* and *Csf2rb* (Fig. 6A). Comparison of MΦ cluster composition in LP and SILTs revealed a loss in the relative abundance of cluster 2 and 3 MΦs in *Csf2*$^{-/-}$ compared with WT (Fig. 6, B and C). Tim-4$^+$ LAMs (cluster 0) were reduced in the LP$^{Csf2-/-}$ (Fig. 6, B and C). We hypothesized that CSF2 deficiency renders colonic monocytes and CCR2$^+$ MΦs unable to differentiate and undergo apoptosis based on CSF2's role as a prosurvival factor for myeloid cells (*48*). An assessment of apoptosis in colonic MΦs revealed an increase in apoptotic Ly6C$^+$ and Tim-4$^-$CD4$^-$ MΦs in *Csf2*$^{-/-}$ mice, the latter likely corresponding to the loss of SAMs in SILT$^{Csf2-/-}$ (Fig. 6D).

CSF2 promotes the transition of monocyte to MΦs in the inflamed brain, specifically by supporting disease-promoting functions in MΦs (*21*). These findings are in contrast to our data showing CSF2-driven pathways in steady-state colonic MΦs. Pathway analysis based on DEGs of each cluster in each region of WT versus *Csf2*$^{-/-}$ mice revealed differences in multiple MΦ clusters, including those devoid of *Csf2ra* or *Csf2rb* mRNAs (Fig. 6, A, E, and F). Within the LP$^{Csf2-/-}$, Tim-4$^+$ LAMs (red) and CCR2$^+$ MΦs (orange) were impaired in cytoskeleton organization, migration, and endocytosis but enriched in proinflammatory processes such as T cell activation, antigen activation, leukocyte-mediated cytotoxicity, and the response to biotic stimuli (Fig. 6E). An even larger number of MΦ clusters were affected in SILT$^{Csf2-/-}$. Similar to LP$^{Csf2-/-}$ Tim-4$^+$ LAMs, homeostasis of SILT$^{Csf2-/-}$ Tim-4$^+$ SAMs (aqua) was impaired as shown by altered synapse pruning and wound healing functions, as well as up-regulated proinflammatory pathways (Fig. 6F). Tim-4$^-$CD4$^+$ MΦs (dark blue) followed these trends toward altered homeostasis and increased inflammation. Conversely, clusters corresponding to monocytes (green) and CCR2$^+$ MΦs (orange) down-regulated pathways involved in response to stimuli and were enriched in pathways related to cell survival, glycolipid catabolism, and protein stabilization in SILT$^{Csf2-/-}$, confirming the increased apoptosis in *Csf2*$^{-/-}$ mice (Fig. 6, D to F). It is possible that CSF2 itself or its effects on MΦ gene expression profiles as described could affect SILT formation and function. This prompted us to quantify SILT numbers and diameters, revealing higher numbers of smaller SILTs in *Csf2*$^{-/-}$ mice (fig. S6A). However, these alterations had no significant impact on the production of immunoglobulin A (IgA) in the colon during steady state (fig. S6B) (*49*, *50*). Instead, mitochondrial homeostasis of SAMs was impaired in *Csf2*$^{-/-}$ animals, indicated by lower ROS production in SILT-associated Ly6C$^+$ monocytes and Tim-4$^-$CD4$^-$ SAMs, as well as reduced mitochondrial membrane potential in CCR2$^+$ SAMs (Fig. 6G and fig. S6C). These data show that CSF2 controls mitochondrial functions implicated in energy generation and antimicrobial activity particularly within SAMs. As a result, *Csf2*$^{-/-}$ colons are enriched in MΦs skewed toward proinflammatory processes, whereas down-regulating functions were attributed to antimicrobial host defense and bioenergy metabolism. Collectively, these findings demonstrate that CSF2-rich SILTs constitute microanatomic niches for the homeostatic development and functional programming of MΦs in the colon.

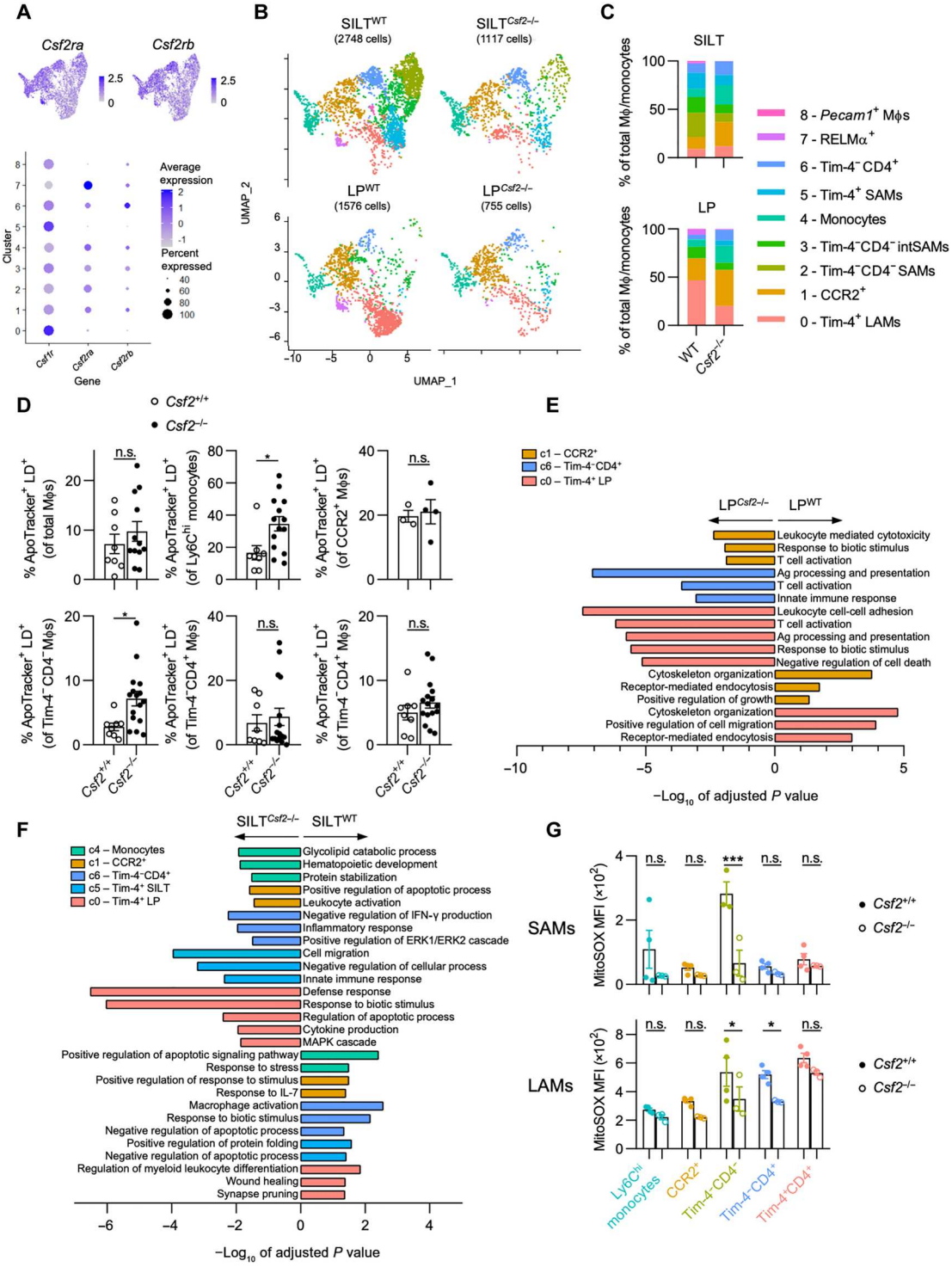


**Fig. 6. CSF2 deficiency results in a loss of Tim-4$^-$CD4$^-$ SAMs and functional dysregulation of colonic MΦs.** (**A**) Feature plots (top) and dot plot (bottom) showing expression of *Csf1r*, *Csf2ra*, and *Csf2rb* in each cluster from the merged data. Color denotes expression level, and dot size indicates percentage of cells within the cluster expressing the gene, as indicated. (**B**) UMAP projection of MΦs/monocytes of each sample. (**C**) Quantification of the relative abundance of each cluster for each sample. (**D**) Quantification of apoptotic cells within each colonic MΦ population in sex-matched littermate WT versus *Csf2*$^{-/-}$ mice by ApoTracker staining, as indicated. (**E** and **F**) Pathway enrichment analysis (gProfiler, GO biological processes) using DEGs differentially regulated between WT versus *Csf2*$^{-/-}$ in (E) LP and (F) SILT for selected clusters, as indicated. Negative values of $-\log_{10}$ of adjusted *P* value indicate up-regulation in *Csf2*$^{-/-}$, and positive values indicate up-regulation in WT. (**G**) MitoSOX MFI for each SAM population (top) and LAM population (bottom) in sex-matched littermate WT versus *Csf2*$^{-/-}$ mice. Each SAM data point represents pooled SILTs from two or three mice. Unpaired Student's *t* test (D) or two-way ANOVA with post hoc Šidák's multiple comparisons test (G) was performed. IFN-γ, interferon-γ; MAPK, mitogen-activated protein kinase; ERK1, extracellular signal–regulated kinase 1.

### CSF2-dependent Tim-4$^-$CD4$^-$ MΦs are required for host defense against enteric infections

ILC3s are central for the innate immune response against attaching and effacing enteric pathogens such as *Citrobacter rodentium*, the murine counterpart of human enteropathogenic *E. coli* (*51*). CSF2 has been implicated in supporting antimicrobial host defense against *C. rodentium* through the modulation of CD11c$^+$ myeloid cells (*52*). In line with this, CD11c-expressing DCs are impaired in their development in *Csf2*$^{-/-}$ mice as previously reported (fig. S7A) (*9*). However, in contrast to previous reports using *C. rodentium* infections, CD11c$^+$MHCII$^+$CD64$^-$ DCs did not significantly differ between *Csf2*$^{-/-}$ and littermate controls after infection, likely because of a CSF2-independent increase in CD103$^-$CD11b$^+$ DCs (fig. S7, B and C). *C. rodentium*–infected mice had elevated levels of luminal ATP$^{ex}$ (fig. S7D). These findings prompted us to revisit whether CSF2-dependent MΦs contribute to the defense against *C. rodentium*.

Tim-4$^-$CD4$^-$ SAMs, the MΦ population most affected in *Csf2*$^{-/-}$ mice, were characterized by their expression of genes related to OXPHOS, high mitochondrial membrane potential, and elevated ROS production, which were affected in the absence of CSF2. We reasoned that inhibition of OXPHOS in WT mice would partly recapitulate the observed mitochondrial alteration in colonic MΦs of *Csf2*$^{-/-}$ mice (Figs. 5 and 6). To validate this hypothesis, we compared *C. rodentium*–infected *Csf2*$^{-/-}$ and littermate control mice treated daily with IACS-010759 (IACS), an established oral inhibitor of OXPHOS, or vehicle control (Fig. 7A). In line with previous reports, *Csf2*$^{-/-}$ mice showed greater weight loss and higher pathogen burden and dissemination compared with their WT littermates despite comparable infection efficiency (Fig. 7, B and C) (*52*). IACS-treated WT mice phenocopied untreated *Csf2*$^{-/-}$ mice, but disease severity was not exacerbated when OXPHOS was blocked in *Csf2*$^{-/-}$ mice (Fig. 7, B and C). IACS acted downstream of CSF2 production by ILC3s, because treatment had no effects on the numbers of total or CSF2-producing ILC3s (fig. S7D). More strikingly, OXPHOS inhibition resulted in a decrease in Tim-4$^-$CD4$^-$ MΦs, recapitulating the lower Tim-4$^-$CD4$^-$ MΦ numbers observed in *Csf2*$^{-/-}$ mice (Fig. 7D and fig. S7E). In line with the characterization of MΦs in *Csf2*$^{-/-}$ mice, OXPHOS inhibition had a major impact on the mitochondrial membrane potential across most colonic MΦ subsets and more specific impact on ROS production in Ly6C$^{hi}$ monocytes and CCR2$^+$ MΦs, immediate precursors of Tim-4$^-$CD4$^-$ MΦs (Fig. 7, E to G). In summary, these data show that CSF2-dependent host defense against enteric pathogens operates via the regulation mitochondrial energy homeostasis and ROS production imprinted preferentially in SAMs.

## DISCUSSION

Intestinal MΦs are critical for gut homeostasis and host defense. Uncovering the mechanisms regulating their developmental and functional heterogeneity is a critical step in our understanding of these cells. Here, we provide a molecular and cellular framework that governs microbiota- and host-regulated MΦ development in the gut. We demonstrate that microbiota-derived ATP$^{ex}$ fuels the production of CSF2 by ILC3s via P2X7R and NLRP3 in myeloid cells and identify SILTs as a distinct niche for CSF2-dependent development and functional programming of SAMs that support antimicrobial defense (fig. S8).

Intestinal SILTs, in contrast to tertiary lymphoid organs (TLOs), form postnatally and mature depending on signals by the gut microbiota (*50*, *53*, *54*). Best known to support B cell maturation, our findings indicate that SILTs constitute a developmental hub for monocyte-derived SAMs that support antimicrobial host defense (*55*). Although ILF-residing *Cxcl13*-expressing MΦs were shown to support IgA-producing B cells during *Salmonella* infection, their development is unlikely to be affected by CSF2, because IgA titers were unchanged in *Csf2*$^{-/-}$ mice (*50*). We show that monocyte transition into SAMs requires CSF2-dependent regulation of their high mitochondrial membrane potential and ROS production to support host defense against infections. However, their role in regulating adaptive immunity within SILTs remains an open question.

Collectively, our findings propose a mechanistic model explaining how the microbiota, irrespective of strain or kingdom, contributes to the steady-state heterogeneity of intestinal MΦs. In contrast to specific bacteria-derived metabolites such as tryptophan or SCFAs, ATP is abundantly produced across all microbial kingdoms. Here, we demonstrate that ATP$^{ex}$ governs the steady-state activation of ILC3s via an NLRP3- and P2X7R-dependent activation of myeloid cells. This is in line with previous reports showing that intestinal MΦs are a major source of steady-state IL-1β and central for the activation of ILC3s (*9*, *25*, *43*). ILC3s do not respond to direct stimulation with ATP$^{ex}$ but secrete CSF2 in response to IL-1β. Tim-4$^+$ MΦs among other myeloid populations coexpressed the highest levels of P2X7R and pro–IL-1β, making them one possible mediator between microbial ATP$^{ex}$ and ILC3 activation. However, *Il1b*, *P2rx7*, and *Nlrp3* transcripts and P2X7R protein were also detected in DCs and other MΦ subpopulations, opening the possibility for collaboration between these myeloid cells to control ILC3-derived CSF2 via IL-1β. Our findings indicate that ATP$^{ex}$, as a measurement for universal microbial energy metabolism, serves as a rheostat for the control of gut MΦ development in the steady state. However, cell stress or death can contribute to increases in ATP$^{ex}$ concentration not originating from the microbiota, which could affect the production of ILC3-derived CSF2. The instability of ATP in the extracellular space and expression of ectonucleotidases by the intestinal epithelium may be a rate-limiting step in the activation of ILC3s and the regulation of MΦ heterogeneity, suggesting a possible feedback loop controlling these interactions.

Although ATP$^{ex}$-mediated activation of the inflammasome drives disease in extraintestinal locations, it constitutes a critical element to tune immune homeostasis in the gut (*56*). In contrast to its redundant and often proinflammatory role in other organs, CSF2 governs the steady-state transition of monocytes to MΦs in the intestine and controls essential homeostatic functions and defense pathways in gut MΦs (*57*). We found that ILC3-derived CSF2 promotes survival and differentiation of monocytes and shapes the metabolic and functional program of MΦs within SILTs. Moreover, SAMs followed a distinct developmental trajectory compared with LAMs, diverging from Tim-4$^-$CD4$^+$ MΦs. Deficiency in *Csf2* resulted in the loss of SAMs and promoted inflammatory pathways in LAMs even if our gene expression analysis suggests a lack of responsiveness to CSF2. This enrichment of inflammatory pathways in *Csf2*-deficient MΦs is possibly the result of a misdirected strategy to reinstate antimicrobial host defense and is of translational relevance, considering the presence of mutations

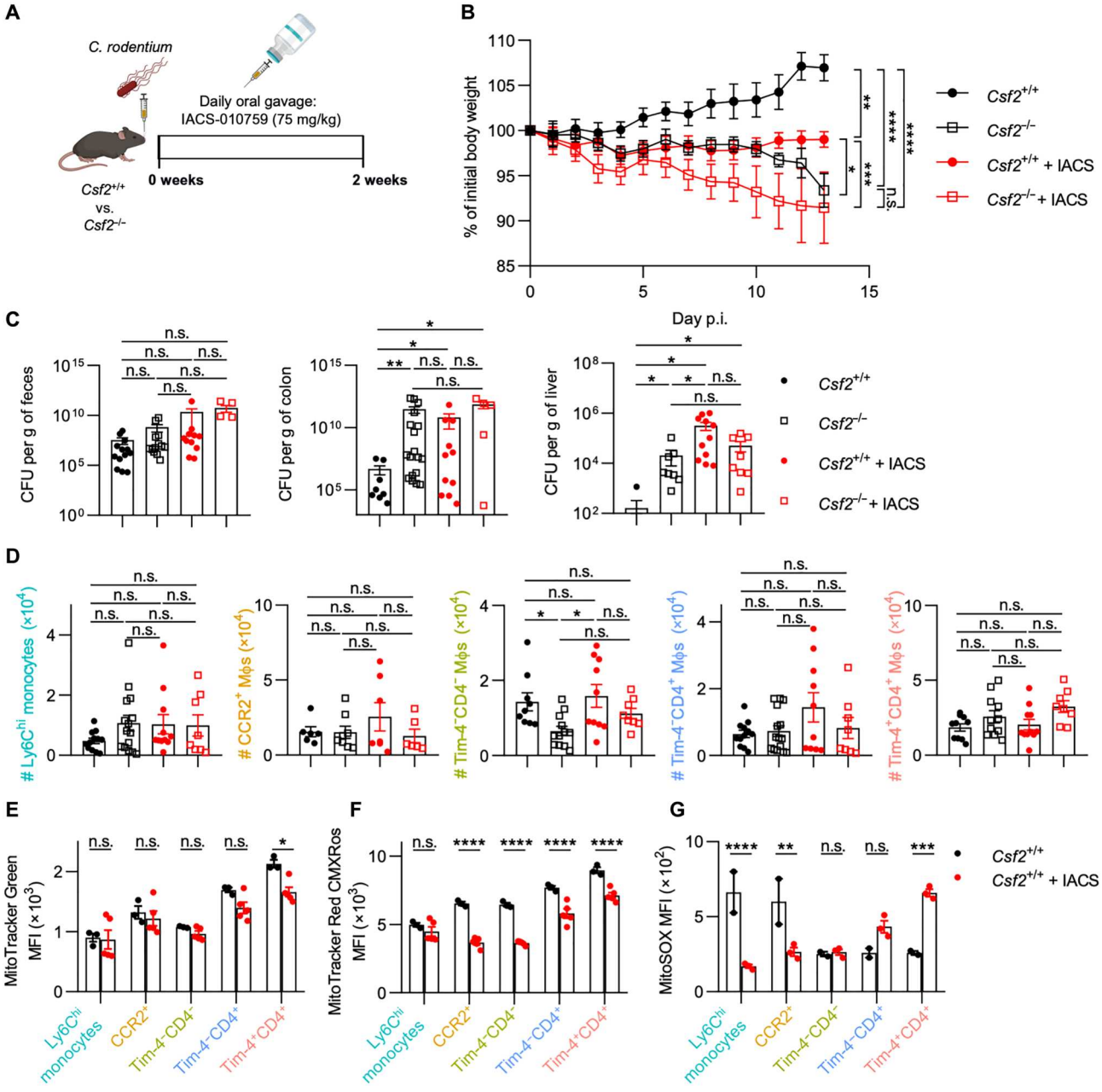


**Fig. 7. Host defense against *C. rodentium* requires CSF2-dependent Tim-4$^{-}$CD4$^{-}$ MΦs and OXPHOS activity.** (**A**) Experimental set-up of *C. rodentium* infection and daily oral treatment of OXPHOS inhibitor IACS-010759 (IACS). (**B**) Body weight was tracked daily during the course of infection. (**C**) Quantification of *C. rodentium* in the feces, colon, and liver at end point. (**D**) Quantification of colonic MΦ populations at end point. (**E**) Mitochondria counts, (**F**) mitochondrial membrane potential, and (**G**) superoxide production of each MΦ population in infected control mice or IACS-treated mice. Mixed-effects analysis with post hoc Šidák's multiple comparisons test (B), one-way ANOVA with post hoc Tukey's test (C and D), or two-way ANOVA with post hoc Šidák's multiple comparisons test (E to G) was performed.

in *CSF2RB* and neutralizing anti-CSF2 autoantibodies in complicated Crohn's disease (CD) (*58*, *59*). Neutralizing anti-human CSF2 autoantibodies precede the onset of CD by several years and are implicated in elevated subclinical inflammation before diagnosis and disease complications at the time of diagnosis (*60*). It remains possible that systemic CSF2 deficiency elicits its effects on the intestinal MΦ population indirectly by perturbing critical systemic homeostasis; however, our studies selectively deleting CSF2 in RORγt-dependent ILC3s, highly enriched in the intestine, suggests an important role of CSF2 in maintaining gut-resident MΦs.

In summary, our results suggest that abrogating the steady-state, microbiota-driven, ILC3-CSF2 niche for intestinal MΦ development and function raises the susceptibility to enteric infections that can serve as a trigger for the onset of CD (*60*). The analysis of MΦs and DCs in *C. rodentium*–infected *Csf2*$^{-/-}$ mice refines previous reports and indicates responsiveness of DCs even in the absence of CSF2, whereas MΦs fail to expand and execute their

antimicrobial activity because of impaired CSF2-dependent OXPHOS and mitochondrial ROS generation. This is in line with a recent report demonstrating OXPHOS as a distinguishing factor for proinflammatory MΦs, with impairment of OXPHOS leading to cellular stress and reduced MΦ numbers, particularly of alveolar MΦs that are also CSF2 dependent (*61*, *62*). Imprinting of these metabolic functions is predominant in monocytes and SAMs, pointing to a need to develop new tools to refine functional characterization of MΦs within distinct microanatomic locations. Collectively, our data identify an underappreciated role for microbe-derived ATP as a regulator of MΦ development within SILTs guided by ILC3-derived CSF2 and classify SILTs as microanatomic niches for MΦ development to constitute an antimicrobial firewall.

## MATERIALS AND METHODS

### Study design

We aimed to identify pathways that integrate microbiota- and host-derived signals into the development and function of intestinal MΦs. We used gnotobiotic and transgenic mouse lines to dissect MΦ ontogeny, myeloid growth factor expression, and gene expression of MΦs within spatial niches. We paired mitochondrial characterization and enteric infections to demonstrate that ILC3-derived CSF2, relying on myeloid purinergic signaling triggered by microbiota-derived ATP, supports the differentiation of monocytes to MΦs in the gut. Experiments across this study were conducted at least two to three times on groups of three to five mice of both sexes using age-matched littermate controls. Sequencing data and code are publicly available, and materials used to generate the data are fully disclosed. Figures include representative experiments or pooled data; no outliers were excluded.

### Animals

All mice were purchased from the Jackson Laboratory and subsequently bred in house under SPF conditions at the University of Toronto, Division of Comparative Medicine. Unless otherwise stated, all experiments were conducted using 8- to 10-week-old age- and sex-matched littermates of both sexes. Germ-free animals were maintained in the gnotobiotic facility at the University of Toronto, Division of Comparative Medicine. To obtain rewilded mice, pet store mice were purchased from High Oak Ranch Ltd. (Baden, ON) and bred in our mouse facility in a containment room (bioBUBBLE Inc., Fort Collins, CO). C57Bl/6 (B6) pups were cohoused with pet store pups from 3 to 7 weeks of age, separated, and subsequently bred. B6 pregnant dams were gavaged with cecal content from pet store female mice 2 to 3 days before delivery. The pups were used to establish a rewilded colony for experiments. *Csf2*$^{\text{flox-tdTomato}}$ (*Csf2*$^{\text{fl}}$) were recently described, crossed to *Vav1*$^{\text{iCre}}$ [B6.Cg-Commd10Tg(Vav1-iCre) A2Kio/J; 008610] or *Rorc*$^{\text{Cre}}$ [B6.FVB-Tg(Rorc-cre)1Litt/J; 022791], and housed at the University of Zurich Laboratory Animal Sciences Center in Zurich, Switzerland (*63*). All other strains were obtained from the Jackson Laboratory. All experiments were approved by the Faculty of Medicine and Pharmacy Animal Care Committee at the University of Toronto (animal use protocols 20011887 and 20012454 to T.M. and 20012400 to A. Mortha) or the cantonal veterinary office of Zurich (permit number ZH134/2019 to C.S.).

### Microbes

All *E. coli* MG1655 strains were provided by T. Conway (Oklahoma State University). *C. rodentium* ICC180 was a gift from D. Philpott (University of Toronto). The plasmid encoding the ATP biosensor (pRSET-AT3.10) was a gift from H. Imamura (Kyoto University).

### Isolation of intestinal LP leukocytes

Colonic or small intestinal LP cells were isolated as previously described (*64*). Briefly, intestines were washed in Hanks′ balanced salt solution (HBSS) plus 5 mM EDTA and 10 mM Hepes to strip the epithelium. Tissues were then minced and shaken at 37°C for 20 min in digestion buffer [HBSS with calcium and magnesium supplemented with 10 mM Hepes, 4% fetal bovine serum, penicillin-streptomycin (Sigma-Aldrich), deoxyribonuclease I (0.5 mg/ml; Sigma-Aldrich), and collagenase (0.5 mg/ml; Sigma-Aldrich)]. Supernatants were collected and enriched for leukocytes using a 40/80% Percoll gradient, after which cells were ready for downstream use. To isolate SILTs, intestines were placed under a Zeiss AxioZoom.V16 fluorescent macroscope for live imaging after epithelium stripping. SILTs were isolated using a 1.25-mm biopsy puncher. SILTs and remaining punched out colons were placed separately into R-10$^{+}$ media until tissue digestion.

### *C. rodentium* infection and pathological assessment

Groups of age- and sex-matched littermates were infected with *C. rodentium* ICC180 [~$2 \times 10^8$ colony-forming units (CFUs)] by oral gavage as previously described (*65*). Mice were weighed daily to monitor disease progression and euthanized at 2 weeks post infection (p.i.) Colons were harvested for LP leukocyte isolation and downstream analysis. CFUs of *C. rodentium* in the feces, colon, and liver were measured on MacConkey agar plates containing kanamycin (100 μg/ml). To minimize contamination, colons were immediately removed of their luminal content and rinsed in PBS before processing, as previously described (*65*). The OXPHOS inhibitor IACS-010759 (Chemietek) was dissolved in dimethyl sulfoxide, diluted in 5% methyl cellulose, and administered (7.5 mg/kg) via oral gavage to experimental groups daily, starting 4 hours before *C. rodentium* infection until the time of analysis.

### Intrarectal application of ATPγS

ATPγS tetralithium salt (4080, Bio-Techne) was dissolved in dd$H_2O$ and immediately stored at −20°C to avoid degradation. For in vivo application, mice were first anesthetized with isoflurane, and a plastic feeding needle lubricated with sterile jelly gel was used to slowly apply 100 μl of ATPγS (12.5 mg/ml) intrarectally, 4 cm into the colon. Mice were held in an inverted position for at least 30 s to ensure solution remained in the colon before removal of the needle. ATPγS was administered to mice daily from day of *E. coli* colonization until the day of analysis. Mice in the control group were administered sterile PBS intrarectally.

### Luminal ATP measurement

Fecal samples were collected, homogenized in PBS plus 0.01% $NaN_3$ using the Omni Bead Ruptor 24, and centrifuged twice (800*g* followed by 10,000*g*) to remove debris and microbes. Supernatants were filtered through a 0.2-μm filter and Amicon Ultra-0.5 centrifugal filter unit (MilliporeSigma) and then analyzed for ATP levels using the ENLITEN ATP Assay System Bioluminescence Detection Kit (Promega) according to the manufacturer′s instructions.

### Colonization of germ-free mice with *E. coli* strains

Groups of age- and sex-matched littermate germ-free mice were orally gavaged with ~$10^3$ CFU of *E. coli* MG1655 WT or *E. coli* MG1655 Δ*narG* Δ*narZ* Δ(*napD-napA*) or ~$10^4$ CFU of *E. coli* MG1655 *Strr* Δ(*atpA-atpG*). Differences in starting CFUs accounted for the slower growth rate of *E. coli* Δ(*atpA-atpG*) to ensure equal colonization efficiency at the time of analysis. Mice were analyzed 1 week later. Fecal pellets were collected both before gavage and at the time of harvest to confirm colonization.

To determine the localization of the *E. coli* strains in vivo, SPF mice were treated with ampicillin (1 g/liter) ad libitum for 1 week via drinking water. Mice were then orally gavaged with *E. coli* MG1655 WT or *E. coli* MG1655 *Strr* Δ(*atpA-atpG*). One week later, fecal content or mucosal scrapings were collected and quantified for ATeam$^+$ bacterial cells.

### scRNA sequencing

#### *Sample preparation*

Colons ($n$ = 5 per group) from age- and sex-matched *Cx3cr1*$^{GFP/+}$ *Ccr2*$^{RFP/+}$ WT versus *Csf2*$^{-/-}$ littermate mice were isolated and stripped of epithelium as detailed above and then placed under a Zeiss AxioZoom.V16 fluorescent macroscope for live imaging. SILTs were identified on the basis of green fluorescent protein (GFP) and red fluorescent protein (RFP) expression and isolated using a 1.25-mm biopsy puncher. SILTs and remaining punched out colons were pooled and placed separately into R-10$^+$ media. Samples were digested and enriched for leukocytes as detailed above. Samples were then enriched for CD11b$^+$ cells using the EasySep Mouse CD11b Positive Selection Kit II (STEMCELL Technologies) as per the manufacturer's protocol. Purified single-cell suspensions (>90% purity) were resuspended in R-10$^+$ media for 10x Genomics scRNA-seq.

#### *Library preparation, sequencing, preprocessing, and quality control*

Single-cell suspensions were prepared and loaded onto the v3 10x Chromium for the generation of sequencing libraries and processing as described by 10x Genomics. CellRanger (10x Genomics) was used to preprocess sequenced cells, align reads, and generate expression matrices. Seurat (v.4.0) was used for all preprocessing, filtering, and downstream analyses (*66*). Low-quality cells expressing fewer than 200 genes were removed. Doublets and dead cells were excluded on the basis of high number of genes (>6000) and high percentage (>9%) of transcripts mapping to mitochondrial genes, respectively. Cells with high percentage (>20%) of transcripts mapping to dissociation-associated genes, as previously described, were also removed (*67*).

### Normalization, dimensionality reduction, clustering, and cell annotation

To remove technical variation, data were normalized using SCTransform, which uses negative binomial regression to normalize the data, find variable features, and scale the data (*68*). The variance-stabilizing transformation method in SCTransform was used to select 3000 highly variable features. Mitochondrial gene percentage and number of counts (nCount_RNA) were regressed out. Dimensionality reduction was performed using principal components analysis (PCA), and an elbow plot was used to determine the number of statistically significant PCs for subsequent clustering. FindNeighbors and FindClusters functions were used to perform graph-based clustering. Nonlinear dimensionality reduction and visualization was performed using the UMAP method. Clusters were identified and annotated on the basis of differential gene expression testing using the Wilcoxon rank sum test, with the following parameters in the FindAllMarkers function: min.pct = 0.25, log fold change (logFC) threshold = 0.25, and adjusted $P$ value < 0.05. For heatmaps, each cluster was downsampled to 50 cells for visualization, showing the top 30 DEGs of each cluster.

MΦ and monocyte clusters were identified on the basis of expression of MΦ markers (*C1qa*, *Csf1r*, *Cx3cr1*, and *Adgre1*) and the absence of DC markers (*Flt3*, *Dpp4*, and *Zbtb46*). These clusters were further subsetted (using the "subset" function), and normalization, dimensionality reduction, and clustering were reperformed as described above to obtain specific MΦ and monocyte clusters. Clusters were identified, annotated, and visualized as described above.

### Differential gene expression

To compare the gene expression of MΦs between WT versus *Csf2*$^{-/-}$ [knockout (KO)] LP and TLO, the "subset" function was used to separate each cluster from each dataset. The FindMarkers function (min.pct = 0.25, logFC threshold = 0.25, and adjusted $P$ value < 0.05) was used to compute differentially up-regulated and down-regulated genes for each cluster in KO relative to WT of each region (e.g., KO LP relative to WT LP and KO TLO relative to WT TLO). Resulting genes were used for subsequent pathway enrichment analysis, as indicated.

### Pathway enrichment analysis

gProfiler functional profiling (https://biit.cs.ut.ee/gprofiler/gost) was used to measure over-representation of target gene list against the annotated gene database of Gene Ontology (GO; www.geneontology.org). Enriched biological processes of GO (BP, 2019) and enriched Kyoto Encyclopedia of Genes and Genomes pathways were identified and ordered on the basis of enrichment scores ($-\log_{10}$ of the adjusted $P$ value).

### Single-cell trajectory analysis

The R package Monocle 3 was used to assess cell trajectories (*69*–*71*). Data previously analyzed with Seurat (v.4.0), as described above, were imported into Monocle 3 for reclustering. Briefly, highly variable genes imported from the Seurat analysis were used for PCA dimensionality reduction, followed by UMAP nonlinear dimensionality reduction and subsequent clustering using Leidan community detection (https://arxiv.org/abs/1802.03426). The number of Monocle clusters was similar to Seurat clusters. This method also generates "partitions" representing groups corresponding to separate trajectories. Cell trajectory was assessed using the "learn_graph" function, which uses the DDRTree method to learn tree-like trajectories and further reduce dimensionality. Data were visualized with UMAP embeddings and trajectories derived within Monocle and overlaid with Seurat clusters.

### Quantification and statistical analysis

Statistical analysis of nonsequencing data was performed with the GraphPad Prism software (GraphPad), with statistical tests detailed in the figure legends. All data are shown as means ± SEM. Significant differences were defined at $P < 0.05$, $^*P < 0.05$, $^{**}P < 0.01$, $^{***}P < 0.001$, and $^{****}P < 0.0001$; n.s., not significant. Unless otherwise

stated, data shown in each figure are representative of at least three independent experiments with at least three sex- and age-matched mice per group per experiment.

## Supplementary Materials

**This PDF file includes:**
Figs. S1 to S8
Tables S1

**Other Supplementary Material for this manuscript includes the following:**
Data file S1
MDAR Reproducibility Checklist

## REFERENCES AND NOTES


1. P. Chiaranunt, S. L. Tai, L. Ngai, A. Mortha, Beyond immunity: Underappreciated functions of intestinal macrophages. *Front. Immunol.* **12**, 749708 (2021).
2. S. A. Dick, A. Wong, H. Hamidzada, S. Nejat, R. Nechanitzky, S. Vohra, B. Mueller, R. Zaman, C. Kantores, L. Aronoff, A. Momen, D. Nechanitzky, W. Y. Li, P. Ramachandran, S. Q. Crome, B. Becher, M. I. Cybulsky, F. Billia, S. Keshavjee, S. Mital, C. S. Robbins, T. W. Mak, S. Epelman, Three tissue resident macrophage subsets coexist across organs with conserved origins and life cycles. *Sci. Immunol.* **7**, eabf7777 (2022).
3. B. Kang, L. J. Alvarado, T. Kim, M. L. Lehmann, H. Cho, J. He, P. Li, B. H. Kim, A. Larochelle, B. L. Kelsall, Commensal microbiota drive the functional diversification of colon macrophages. *Mucosal Immunol.* **13**, 216–229 (2020).
4. T. N. Shaw, S. A. Houston, K. Wemyss, H. M. Bridgeman, T. A. Barbera, T. Zangerle-Murray, P. Strangward, A. J. L. Ridley, P. Wang, S. Tamoutounour, J. E. Allen, J. E. Konkel, J. R. Grainger, Tissue-resident macrophages in the intestine are long lived and defined by Tim-4 and CD4 expression. *J. Exp. Med.* **215**, 1507–1518 (2018).
5. Z. Liu, Y. Gu, S. Chakarov, C. Bleriot, I. Kwok, X. Chen, A. Shin, W. Huang, R. J. Dress, C. A. Dutertre, A. Schlitzer, J. Chen, L. G. Ng, H. Wang, Z. Liu, B. Su, F. Ginhoux, Fate mapping via Ms4a3-expression history traces monocyte-derived cells. *Cell* **178**, 1509–1525.e19 (2019).
6. S. De Schepper, S. Verheijden, J. Aguilera-Lizarraga, M. F. Viola, W. Boesmans, N. Stakenborg, I. Voytyuk, I. Schmidt, B. Boeckx, I. D. de Casterlé, V. Baekelandt, E. G. Dominguez, M. Mack, I. Depoortere, B. De Strooper, B. Sprangers, U. Himmelreich, S. Soenen, M. Guilliams, P. V. Berghe, E. Jones, D. Lambrechts, G. Boeckxstaens, Self-maintaining gut macrophages are essential for intestinal homeostasis. *Cell* **175**, 400–415.e13 (2018).
7. P. A. Muller, B. Koscsó, G. M. Rajani, K. Stevanovic, M. L. Berres, D. Hashimoto, A. Mortha, M. Leboeuf, X. M. Li, D. Mucida, E. R. Stanley, S. Dahan, K. G. Margolis, M. D. Gershon, M. Merad, M. Bogunovic, Crosstalk between muscularis macrophages and enteric neurons regulates gastrointestinal motility. *Cell* **158**, 300–313 (2014).
8. F. Matheis, P. A. Muller, C. L. Graves, I. Gabanyi, Z. J. Kerner, D. Costa-Borges, T. Ahrends, P. Rosenstiel, D. Mucida, Adrenergic signaling in muscularis macrophages limits infection-induced neuronal loss. *Cell* **180**, 64–78.e16 (2020).
9. A. Mortha, A. Chudnovskiy, D. Hashimoto, M. Bogunovic, S. P. Spencer, Y. Belkaid, M. Merad, Microbiota-dependent crosstalk between macrophages and ILC3 promotes intestinal homeostasis. *Science* **343**, 1249288 (2014).
10. C. Danne, G. Ryzhakov, M. Martínez-López, N. E. Ilott, F. Franchini, F. Cuskin, E. C. Lowe, S. J. Bullers, J. S. C. Arthur, F. Powrie, A large polysaccharide produced by helicobacter hepaticus induces an anti-inflammatory gene signature in macrophages. *Cell Host Microbe* **22**, 733–745.e5 (2017).
11. P. V. Chang, L. Hao, S. Offermanns, R. Medzhitov, The microbial metabolite butyrate regulates intestinal macrophage function via histone deacetylase inhibition. *Proc. Natl. Acad. Sci. U.S.A.* **111**, 2247–2252 (2014).
12. J. Schulthess, S. Pandey, M. Capitani, K. C. Rue-Albrecht, I. Arnold, F. Franchini, A. Chomka, N. E. Ilott, D. G. W. Johnston, E. Pires, J. McCullagh, S. N. Sansom, C. V. Arancibia-Cárcamo, H. H. Uhlig, F. Powrie, The short chain fatty acid butyrate imprints an antimicrobial program in macrophages. *Immunity* **50**, 432–445.e7 (2019).
13. C. Goudot, A. Coillard, A. C. Villani, P. Gueguen, A. Cros, S. Sarkizova, T. L. Tang-Huau, M. Bohec, S. Baulande, N. Hacohen, S. Amigorena, E. Segura, Aryl hydrocarbon receptor controls monocyte differentiation into dendritic cells versus macrophages. *Immunity* **47**, 582–596.e6 (2017).
14. P. Chiaranunt, K. Burrows, L. Ngai, E. Y. Cao, H. Liang, S. L. Tai, C. J. Streutker, S. E. Girardin, A. Mortha, NLRP1B and NLRP3 control the host response following colonization with the commensal protist tritrichomonas musculis. *J. Immunol.* **208**, 1782–1789 (2022).
15. M. D. Witmer-Pack, D. A. Hughes, G. Schuler, L. Lawson, A. McWilliam, K. Inaba, R. M. Steinman, S. Gordon, Identification of macrophages and dendritic cells in the osteopetrotic (op/op) mouse. *J. Cell Sci.* **104**, 1021–1029 (1993).
16. A. Sehgal, D. S. Donaldson, C. Pridans, K. A. Sauter, D. A. Hume, N. A. Mabbott, The role of CSF1R-dependent macrophages in control of the intestinal stem-cell niche. *Nat. Commun.* **9**, 1272 (2018).
17. X. M. Dai, G. R. Ryan, A. J. Hapel, M. G. Dominguez, R. G. Russell, S. Kapp, V. Sylvestre, E. R. Stanley, Targeted disruption of the mouse colony-stimulating factor 1 receptor gene results in osteopetrosis, mononuclear phagocyte deficiency, increased primitive progenitor cell frequencies, and reproductive defects. *Blood* **99**, 111–120 (2002).
18. M. Guilliams, I. de Kleer, S. Henri, S. Post, L. Vanhoutte, S. de Prijck, K. Deswarte, B. Malissen, H. Hammad, B. N. Lambrecht, Alveolar macrophages develop from fetal monocytes that differentiate into long-lived cells in the first week of life via GM-CSF. *J. Exp. Med.* **210**, 1977–1992 (2013).
19. M. Greter, I. Lelios, P. Pelczar, G. Hoeffel, J. Price, M. Leboeuf, T. M. Kündig, K. Frei, F. Ginhoux, M. Merad, B. Becher, Stroma-derived interleukin-34 controls the development and maintenance of langerhans cells and the maintenance of microglia. *Immunity* **37**, 1050–1060 (2012).
20. A. Schridde, C. C. Bain, J. U. Mayer, J. Montgomery, E. Pollet, B. Denecke, S. W. F. Milling, S. J. Jenkins, M. Dalod, S. Henri, B. Malissen, O. Pabst, A. Mcl Mowat, Tissue-specific differentiation of colonic macrophages requires TGFβ receptor-mediated signaling. *Mucosal Immunol.* **10**, 1387–1399 (2017).
21. A. Amorim, D. de Feo, E. Friebel, F. Ingelfinger, C. D. Anderfuhren, S. Krishnarajah, M. Andreadou, C. A. Welsh, Z. Liu, F. Ginhoux, M. Greter, B. Becher, IFNγ and GM-CSF control complementary differentiation programs in the monocyte-to-phagocyte transition during neuroinflammation. *Nat. Immunol.* **23**, 217–228 (2022).
22. C. C. Bain, A. Bravo-Blas, C. L. Scott, E. Gomez Perdiguero, F. Geissmann, S. Henri, B. Malissen, L. C. Osborne, D. Artis, A. M. I. Mowat, Constant replenishment from circulating monocytes maintains the macrophage pool in the intestine of adult mice. *Nat. Immunol.* **15**, 929–937 (2014).
23. H. Moura Silva, J. Z. Kitoko, C. P. Queiroz, L. Kroehling, F. Matheis, K. L. Yang, B. S. Reis, C. Ren-Fielding, D. R. Littman, M. T. Bozza, D. Mucida, J. J. Lafaille, c-MAF-dependent perivascular macrophages regulate diet-induced metabolic syndrome. *Sci. Immunol.* **6**, eabg7506 (2021).
24. F. Guendel, M. Kofoed-Branzk, K. Gronke, C. Tizian, M. Witkowski, H. W. Cheng, G. A. Heinz, F. Heinrich, P. Durek, P. S. Norris, C. F. Ware, C. Ruedl, S. Herold, K. Pfeffer, T. Hehlgans, A. Waisman, B. Becher, A. D. Giannou, S. Brachs, K. Ebert, Y. Tanriver, B. Ludewig, M. F. Mashreghi, A. A. Kruglov, A. Diefenbach, Group 3 innate lymphoid cells program a distinct subset of IL-22BP-producing dendritic cells demarcating solitary intestinal lymphoid tissues. *Immunity* **53**, 1015–1032.e8 (2020).
25. T. Castro-Dopico, A. Fleming, T. W. Dennison, J. R. Ferdinand, K. Harcourt, B. J. Stewart, Z. Cader, Z. K. Tuong, C. Jing, L. S. C. Lok, R. J. Mathews, A. Portet, A. Kaser, S. Clare, M. R. Clatworthy, GM-CSF calibrates macrophage defense and wound healing programs during intestinal infection and inflammation. *Cell Rep.* **32**, 107857 (2020).
26. C. L. Scott, F. Zheng, P. de Baetselier, L. Martens, Y. Saeys, S. de Prijck, S. Lippens, C. Abels, S. Schoonooghe, G. Raes, N. Devoogdt, B. N. Lambrecht, A. Beschin, M. Guilliams, Bone marrow-derived monocytes give rise to self-renewing and fully differentiated Kupffer cells. *Nat. Commun.* **7**, 10321 (2016).
27. I. Theurl, I. Hilgendorf, M. Nairz, P. Tymoszuk, D. Haschka, M. Asshoff, S. He, L. M. S. Gerhardt, T. A. W. Holderried, M. Seifert, S. Sopper, A. M. Fenn, A. Anzai, S. Rattik, C. McAlpine, M. Theurl, P. Wieghofer, Y. Iwamoto, G. F. Weber, N. K. Harder, B. G. Chousterman, T. L. Arvedson, M. McKee, F. Wang, O. M. D. Lutz, E. Rezoagli, J. L. Babitt, L. Berra, M. Prinz, M. Nahrendorf, G. Weiss, R. Weissleder, H. Y. Lin, F. K. Swirski, On-demand erythrocyte disposal and iron recycling requires transient macrophages in the liver. *Nat. Med.* **22**, 945–951 (2016).
28. C. Bleriot, S. Chakarov, F. Ginhoux, Determinants of resident tissue macrophage identity and function. *Immunity* **52**, 957–970 (2020).
29. K. A. Knoop, J. K. Gustafsson, K. G. McDonald, D. H. Kulkarni, P. E. Coughlin, S. McCrate, D. Kim, C. S. Hsieh, S. P. Hogan, C. O. Elson, P. I. Tarr, R. D. Newberry, Microbial antigen encounter during a preweaning interval is critical for tolerance to gut bacteria. *Sci. Immunol.* **2**, eaao1314 (2017).
30. A. Chudnovskiy, A. Mortha, V. Kana, A. Kennard, J. D. Ramirez, A. Rahman, R. Remark, I. Mogno, R. Ng, S. Gnjatic, E. A. D. Amir, A. Solovyov, B. Greenbaum, J. Clemente, J. Faith, Y. Belkaid, M. E. Grigg, M. Merad, Host-protozoan interactions protect from mucosal infections through activation of the inflammasome. *Cell* **167**, 444–456.e14 (2016).
31. M. Guilliams, G. R. Thierry, J. Bonnardel, M. Bajenoff, Establishment and maintenance of the macrophage niche. *Immunity* **52**, 434–451 (2020).

32. H. Hamada, T. Hiroi, Y. Nishiyama, H. Takahashi, Y. Masunaga, S. Hachimura, S. Kaminogawa, H. Takahashi-Iwanaga, T. Iwanaga, H. Kiyono, H. Yamamoto, H. Ishikawa, Identification of multiple isolated lymphoid follicles on the antimesenteric wall of the mouse small intestine. *J. Immunol.* **168**, 57–64 (2002).
33. M. Blaut, T. Clavel, Metabolic diversity of the intestinal microbiota: Implications for health and disease. *J. Nutr.* **137**, 751S–755S (2007).
34. M. L. Patnode, J. L. Guruge, J. J. Castillo, G. A. Couture, V. Lombard, N. Terrapon, B. Henrissat, C. B. Lebrilla, J. I. Gordon, Strain-level functional variation in the human gut microbiota based on bacterial binding to artificial food particles. *Cell Host Microbe* **29**, 664–673.e5 (2021).
35. K. Atarashi, J. Nishimura, T. Shima, Y. Umesaki, M. Yamamoto, M. Onoue, H. Yagita, N. Ishii, R. Evans, K. Honda, K. Takeda, ATP drives lamina propria $T_H17$ cell differentiation. *Nature* **455**, 808–812 (2008).
36. L. Perruzza, G. Gargari, M. Proietti, B. Fosso, A. M. D'Erchia, C. E. Faliti, T. Rezzonico-Jost, D. Scribano, L. Mauri, D. Colombo, G. Pellegrini, A. Moregola, C. Mooser, G. Pesole, M. Nicoletti, G. D. Norata, M. B. Geuking, K. D. McCoy, S. Guglielmetti, F. Grassi, T follicular helper cells promote a beneficial gut ecosystem for host metabolic homeostasis by sensing microbiota-derived extracellular ATP. *Cell Rep.* **18**, 2566–2575 (2017).
37. R. Mempin, H. Tran, C. Chen, H. Gong, K. Kim Ho, S. Lu, Release of extracellular ATP by bacteria during growth. *BMC Microbiol.* **13**, 301 (2013).
38. S. A. Jones, F. Z. Chowdhury, A. J. Fabich, A. Anderson, D. M. Schreiner, A. L. House, S. M. Autieri, M. P. Leatham, J. J. Lins, M. Jorgensen, P. S. Cohen, T. Conway, Respiration of Escherichia coli in the mouse intestine. *Infect. Immun.* **75**, 4891–4899 (2007).
39. H. Imamura, K. P. Huynh Nhat, H. Togawa, K. Saito, R. Iino, Y. Kato-Yamada, T. Nagai, H. Noji, Visualization of ATP levels inside single living cells with fluorescence resonance energy transfer-based genetically encoded indicators. *Proc. Natl. Acad. Sci. U.S.A.* **106**, 15651–15656 (2009).
40. S. Hapfelmeier, M. A. E. Lawson, E. Slack, J. K. Kirundi, M. Stoel, M. Heikenwalder, J. Cahenzli, Y. Velykoredko, M. L. Balmer, K. Endt, M. B. Geuking, R. Curtiss III, K. D. McCoy, A. J. Macpherson, Reversible microbial colonization of germ-free mice reveals the dynamics of IgA immune responses. *Science* **328**, 1705–1709 (2010).
41. A. J. Macpherson, T. Uhr, Induction of protective IgA by intestinal dendritic cells carrying commensal bacteria. *Science* **303**, 1662–1665 (2004).
42. N. Satoh-Takayama, C. A. J. Vosshenrich, S. Lesjean-Pottier, S. Sawa, M. Lochner, F. Rattis, J. J. Mention, K. Thiam, N. Cerf-Bensussan, O. Mandelboim, G. Eberl, J. P. di Santo, Microbial flora drives interleukin 22 production in intestinal $NKp46^+$ cells that provide innate mucosal immune defense. *Immunity* **29**, 958–970 (2008).
43. M. H. Shaw, N. Kamada, Y. G. Kim, G. Nunez, Microbiota-induced IL-1β, but not IL-6, is critical for the development of steady-state TH17 cells in the intestine. *J. Exp. Med.* **209**, 251–258 (2012).
44. D. Perregaux, C. A. Gabel, Interleukin-1 beta maturation and release in response to ATP and nigericin. Evidence that potassium depletion mediated by these agents is a necessary and common feature of their activity. *J. Biol. Chem.* **269**, 15195–15203 (1994).
45. J. Satoh, Y. Kino, N. Asahina, M. Takitani, J. Miyoshi, T. Ishida, Y. Saito, TMEM119 marks a subset of microglia in the human brain. *Neuropathology* **36**, 39–49 (2016).
46. R. Sankowski, C. Böttcher, T. Masuda, L. Geirsdottir, Sagar, E. Sindram, T. Seredenina, A. Muhs, C. Scheiwe, M. J. Shah, D. H. Heiland, O. Schnell, D. Grün, J. Priller, M. Prinz, Mapping microglia states in the human brain through the integration of high-dimensional techniques. *Nat. Neurosci.* **22**, 2098–2110 (2019).
47. N. A. Scott, M. A. E. Lawson, R. J. Hodgetts, G. le Gall, L. J. Hall, E. R. Mann, Macrophage metabolism in the intestine is compartment specific and regulated by the microbiota. *Immunology* **166**, 138–152 (2022).
48. C. K. Wan, J. Oh, P. Li, E. E. West, E. A. Wong, A. B. Andraski, R. Spolski, Z. X. Yu, J. He, B. L. Kelsall, W. J. Leonard, The cytokines IL-21 and GM-CSF have opposing regulatory roles in the apoptosis of conventional dendritic cells. *Immunity* **38**, 514–527 (2013).
49. S. Velaga, H. Herbrand, M. Friedrichsen, T. Jiong, M. Dorsch, M. W. Hoffmann, R. Förster, O. Pabst, Chemokine receptor CXCR5 supports solitary intestinal lymphoid tissue formation, B cell homing, and induction of intestinal IgA responses. *J. Immunol.* **182**, 2610–2619 (2009).
50. B. Koscsó, S. Kurapati, R. R. Rodrigues, J. Nedjic, K. Gowda, C. Shin, C. Soni, A. Z. Ashraf, I. Purushothaman, M. Palisoc, S. Xu, H. Sun, S. B. Chodisetti, E. Lin, M. Mack, Y. I. Kawasawa, P. He, Z. S. M. Rahman, I. Aifantis, N. Shulzhenko, A. Morgun, M. Bogunovic, Gut-resident $CX3CR1^{hi}$ macrophages induce tertiary lymphoid structures and IgA response in situ. *Sci. Immunol.* **5**, eaax0062 (2020).
51. C. Song, J. S. Lee, S. Gilfillan, M. L. Robinette, R. D. Newberry, T. S. Stappenbeck, M. Mack, M. Cella, M. Colonna, Unique and redundant functions of $NKp46^+$ ILC3s in models of intestinal inflammation. *J. Exp. Med.* **212**, 1869–1882 (2015).
52. Y. Hirata, L. Egea, S. M. Dann, L. Eckmann, M. F. Kagnoff, GM-CSF-facilitated dendritic cell recruitment and survival govern the intestinal mucosal response to a mouse enteric bacterial pathogen. *Cell Host Microbe* **7**, 151–163 (2010).
53. G. Eberl, M. Lochner, The development of intestinal lymphoid tissues at the interface of self and microbiota. *Mucosal Immunol.* **2**, 478–485 (2009).
54. A. E. Overacre-Delgoffe, H. J. Bumgarner, A. R. Cillo, A. H. P. Burr, J. T. Tometich, A. Bhattacharjee, T. C. Bruno, D. A. A. Vignali, T. W. Hand, Microbiota-specific T follicular helper cells drive tertiary lymphoid structures and anti-tumor immunity against colorectal cancer. *Immunity* **54**, 2812–2824.e4 (2021).
55. M. Tsuji, K. Suzuki, H. Kitamura, M. Maruya, K. Kinoshita, I. I. Ivanov, K. Itoh, D. R. Littman, S. Fagarasan, Requirement for lymphoid tissue-inducer cells in isolated follicle formation and T cell-independent immunoglobulin A generation in the gut. *Immunity* **29**, 261–271 (2008).
56. E. Aganna, F. Martinon, P. N. Hawkins, J. B. Ross, D. C. Swan, D. R. Booth, H. J. Lachmann, A. Bybee, R. Gaudet, P. Woo, C. Feighery, F. E. Cotter, M. Thome, G. A. Hitman, J. Tschopp, M. McDermott, Association of mutations in the NALP3/CIAS1/PYPAF1 gene with a broad phenotype including recurrent fever, cold sensitivity, sensorineural deafness, and AA amyloidosis. *Arthritis Rheum.* **46**, 2445–2452 (2002).
57. A. A. Achuthan, K. M. C. Lee, J. A. Hamilton, Targeting GM-CSF in inflammatory and autoimmune disorders. *Semin. Immunol.* **54**, 101523 (2021).
58. X. Han, K. Uchida, I. Jurickova, D. Koch, T. Willson, C. Samson, E. Bonkowski, A. Trauernicht, M. O. Kim, G. Tomer, M. Dubinsky, S. Plevy, S. Kugathsan, B. C. Trapnell, L. A. Denson, Granulocyte-macrophage colony-stimulating factor autoantibodies in murine ileitis and progressive ileal Crohn's disease. *Gastroenterology* **136**, 1261–1271.e3 (2009).
59. L. S. Chuang, N. Villaverde, K. Y. Hui, A. Mortha, A. Rahman, A. P. Levine, T. Haritunians, S. M. Evelyn Ng, W. Zhang, N. Y. Hsu, J. A. Facey, T. Luong, H. Fernandez-Hernandez, D. Li, M. Rivas, E. R. Schiff, A. Gusev, L. P. Schumm, B. M. Bowen, Y. Sharma, K. Ning, R. Remark, S. Gnjatic, P. Legnani, J. George, B. E. Sands, J. M. Stempak, L. W. Datta, S. Lipka, S. Katz, A. S. Cheifetz, N. Barzilai, N. Pontikos, C. Abraham, M. J. Dubinsky, S. Targan, K. Taylor, J. I. Rotter, E. J. Scherl, R. J. Desnick, M. T. Abreu, H. Zhao, G. Atzmon, I. Pe'er, S. Kugathasan, H. Hakonarson, J. L. McCauley, T. Lencz, A. Darvasi, V. Plagnol, M. S. Silverberg, A. M. Muise, S. R. Brant, M. J. Daly, A. W. Segal, R. H. Duerr, M. Merad, D. P. B. McGovern, I. Peter, J. H. Cho, A frameshift in CSF2RB predominant among Ashkenazi jews increases risk for Crohn's disease and reduces monocyte signaling via GM-CSF. *Gastroenterology* **151**, 710–723.e2 (2016).
60 . A. Mortha, R. Remark, D. M. Del Valle, L.-S. Chuang, Z. Chai, I. Alves, C. Azevedo, J. Gaifem, J. Martin, F. Petralia, K. Tuballes, V. Barcessat, S. L. Tai, H.-H. Huang, I. Laface, Y. A. Jerez, G. Boschetti, N. Villaverde, M. D. Wang, U. M. Korie, J. Murray, R.-S. Choung, T. Sato, R. M. Laird, S. Plevy, A. Rahman, J. Torres, C. Porter, M. S. Riddle, E. Kenigsberg, S. S. Pinho, J. H. Cho, M. Merad, J.-F. Colombel, S. Gnjatic, Neutralizing anti-granulocyte macrophage-colony stimulating factor autoantibodies recognize post-translational glycosylations on granulocyte macrophage-colony stimulating factor years before diagnosis and predict complicated Crohn's disease. *Gastroenterology* **163**, 659-670 (2022).
61. G. Dranoff, A. D. Crawford, M. Sadelain, B. Ream, A. Rashid, R. T. Bronson, G. R. Dickersin, C. J. Bachurski, E. L. Mark, J. A. Whitsett, R. C. Mulligan, Involvement of granulocyte-macrophage colony-stimulating factor in pulmonary homeostasis. *Science* **264**, 713–716 (1994).
62. S. K. Wculek, I. Heras-Murillo, A. Mastrangelo, D. Mañanes, M. Galán, V. Miguel, A. Curtabbi, C. Barbas, N. S. Chandel, J. A. Enríquez, S. Lamas, D. Sancho, Oxidative phosphorylation selectively orchestrates tissue macrophage homeostasis. *Immunity* **56**, 516–530.e9 (2023).
63. J. Gschwend, S. P. M. Sherman, F. Ridder, X. Feng, H. E. Liang, R. M. Locksley, B. Becher, C. Schneider, Alveolar macrophages rely on GM-CSF from alveolar epithelial type 2 cells before and after birth. *J. Exp. Med.* **218**, e20210745 (2021).
64. P. Chiaranunt, K. Burrows, L. Ngai, A. Mortha, Isolation of mononuclear phagocytes from the mouse gut. *Methods Enzymol.* **632**, 67–90 (2020).
65. N. Bouladoux, O. J. Harrison, Y. Belkaid, The mouse model of infection with *Citrobacter rodentium*. *Curr. Protoc. Immunol.* **119**, 19.1511–19.15.25 (2017).
66. Y. Hao, S. Hao, E. Andersen-Nissen, W. M. Mauck III, S. Zheng, A. Butler, M. J. Lee, A. J. Wilk, C. Darby, M. Zager, P. Hoffman, M. Stoeckius, E. Papalexi, E. P. Mimitou, J. Jain, A. Srivastava, T. Stuart, L. M. Fleming, B. Yeung, A. J. Rogers, J. M. McElrath, C. A. Blish, R. Gottardo, P. Smibert, R. Satija, Integrated analysis of multimodal single-cell data. *Cell* **184**, 3573–3587.e29 (2021).
67. C. H. O'Flanagan, K. R. Campbell, A. W. Zhang, F. Kabeer, J. L. P. Lim, J. Biele, P. Eirew, D. Lai, A. M. Pherson, E. Kong, C. Bates, K. Borkowski, M. Wiens, B. Hewitson, J. Hopkins, J. Pham, N. Ceglia, R. Moore, A. J. Mungall, J. N. M. Alpine; CRUK IMAXT Grand Challenge Team, S. P. Shah, S. Aparicio, Dissociation of solid tumor tissues with cold active protease for single-cell RNA-seq minimizes conserved collagenase-associated stress responses. *Genome Biol.* **20**, 210 (2019).
68. C. Hafemeister, R. Satija, Normalization and variance stabilization of single-cell RNA-seq data using regularized negative binomial regression. *Genome Biol.* **20**, 296 (2019).

69. C. Trapnell, D. Cacchiarelli, J. Grimsby, P. Pokharel, S. Li, M. Morse, N. J. Lennon, K. J. Livak, T. S. Mikkelsen, J. L. Rinn, The dynamics and regulators of cell fate decisions are revealed by pseudotemporal ordering of single cells. *Nat. Biotechnol.* **32**, 381–386 (2014).
70. X. Qiu, Q. Mao, Y. Tang, L. Wang, R. Chawla, H. A. Pliner, C. Trapnell, Reversed graph embedding resolves complex single-cell trajectories. *Nat. Methods* **14**, 979–982 (2017).
71. J. Cao, M. Spielmann, X. Qiu, X. Huang, D. M. Ibrahim, A. J. Hill, F. Zhang, S. Mundlos, L. Christiansen, F. J. Steemers, C. Trapnell, J. Shendure, The single-cell transcriptional landscape of mammalian organogenesis. *Nature* **566**, 496–502 (2019).

**Acknowledgments:** We thank all members of #theonlylabever for the support and discussion. We acknowledge the support by the University of Toronto, Temerty Faculty of Medicine Flow Cytometry Core facility, the 10x Genomics staff at the Princess Margaret Genomics Centre, and the Division for Comparative Medicine. We wish to thank J.-C. Zúñiga-Pflücker and A. Gehring for the critical reading of the manuscript. **Funding:** This study was supported by an Ontario Trillium Scholarship and Vanier Canada Graduate Scholarship–NSERC (P.C.). K.B. is supported by a Canadian Institutes of Health Research (CIHR) Banting Postdoctoral Fellowship Program and the Canadian Allergy, Asthma and Immunology Foundation (CAAIF) and Takeda Canada. L.N. is funded by an Ontario Graduate Scholarship and a NSERC-PGS award. S.L.T. is a recipient of the Dr. Edward Ketchum Graduate Student Scholarship and the Canada Graduate Scholarships–Master's (CGS M) award. H.H. is supported by the Vanier Canada Graduate Scholarship–CIHR. C.S. is supported by the Swiss National Science Foundation (Eccellenza grant 194216), the Peter Hans Hofschneider Professorship for Molecular Medicine, and the SwissLife Jubiläumsstiftung. C.S. and J.G. are supported by the Research Fund of the Swiss Lung Association, Bern. J.G. is an awardee of the UZH Candoc. T.M. is supported by a Canada Research Chair in NKT cell Immunobiology, a CIHR grant (PJT-175055), and a Canada Foundation for Innovation Physical Infrastructure Grant (29186). A. Mortha is supported by the Canadian Foundation for Innovation John R. Evans Leaders Fund, the CIHR (PJT-388337, 6210100847, and 6210100850), and a NSERC-Discovery Grant (RGPIN-2019-04521). A. Mortha is the Tier 2 Canadian Research Chair in Mucosal Immunology and supported by the Tier 2 CRC-CIHR program (CRC-2021-00511). **Author contributions:** Conceptualization: P.C. and A. Mortha. Methodology: P.C. and A. Mortha. Software: P.C. and H.H. Investigation: P.C., K.B., L.N., E.Y.C., S.L.T., H.L., J.G., P.F., A.W., M.K., T.D., A. Momen, and S.M.L. Writing—original draft: P.C. and A. Mortha. Writing—review and editing: P.C. and A. Mortha. Funding acquisition: A. Mortha. Resources: T.M., T.C., H.I., C.S., and S.E. Supervision: A. Mortha. **Competing interests:** The authors declare that they have no competing interests. **Data and materials availability:** Sequencing data have been deposited on NCBI GEO under accession no. GSE231371. Information required to reanalyze the data reported are available via https://doi.org/10.5281/zenodo.7883947. All other data needed to support the conclusions of the paper are present in the paper or the Supplementary Materials.

Submitted 18 April 2022
Resubmitted 13 February 2023
Accepted 7 July 2023
Published 4 August 2023
10.1126/sciimmunol.abq4573

Science Immunology

# Microbial energy metabolism fuels an intestinal macrophage niche in solitary isolated lymphoid tissues through purinergic signaling

Pailin Chiaranunt, Kyle Burrows, Louis Ngai, Siu Ling Tai, Eric Y. Cao, Helen Liang, Homaira Hamidzada, Anthony Wong, Julia Gschwend, Pascal Flüchter, Meggie Kuypers, Tijana Despot, Abdul Momen, Sung Min Lim, Thierry Mallevaey, Christoph Schneider, Tyrrell Conway, Hiromi Imamura, Slava Epelman, and Arthur Mortha

*Sci. Immunol.* **8** (86), eabq4573. DOI: 10.1126/sciimmunol.abq4573







*Science Immunology* (ISSN 2470-9468) is published by the American Association for the Advancement of Science. 1200 New York Avenue NW, Washington, DC 20005. The title *Science Immunology* is a registered trademark of AAAS.